Univerzita Karlova

Přírodovědecká fakulta

Studijní program: Klinická a toxikologická analýza

Studijní obor: Klinická a toxikologická analýza

Ivana Dobiášová

Syntéza a charakterizace zeolitů s kontrolovaným umístěním aktivních míst
Synthesis and characterization of zeolites with controllable location of active sites

Typ závěrečné práce:

Bakalářská práce

Vedoucí práce

Mariya Shamzhy, Ph.D.

Praha 2023

Charles University

Faculty of Science

Study program: Clinical and toxicological analysis

Branch of study: Clinical and toxicological analysis

Ivana Dobiášová

Synthesis and characterization of zeolites with controllable location of active sites

Syntéza a charakterizace zeolitů s kontrolovaným umístěním aktivních míst

Type of thesis

Bachelor´s thesis

Supervisor:

Mariya Shamzhy, Ph.D.

Prague 2023

Prohlášení:

Prohlašuji, že jsem závěrečnou práci zpracovala samostatně a že jsem uvedla všechny použité informační zdroje a literaturu. Tato práce ani její podstatná část nebyla předložena k získání jiného nebo stejného akademického titulu.

V Praze: Podpis:

Acknowledgement

Abstract

This bachelor thesis focusses on the synthesis, post-synthesis modification, and comprehensive characterization of two series of zeolites based on IWW and ITH topologies. The investigated zeolite structures were chosen because their frameworks contain d4r units preferentially occupied by Ge atoms, which can be substituted for various catalytically active metal sites such as Al, Ti, and Sn by post-synthesis degermanation/metallation.

To study the influence of the chemical composition of the parent germanosilicate on the concentration and accessibility of the incorporated Al-, Ti- and Sn-associated acid sites, IWW and ITH were hydrothermally synthesized with different amounts of germanium in the reaction mixture (Si/Ge = 4 – 10 for IWW and Si/Ge = 10 – 30 for ITH) and used for post-synthesis Ge- for-metal substitution.

X-ray diffraction (XRD) was used to verify the structure of the synthesized zeolites; chemical analysis identified their elemental composition; nitrogen physisorption was used to determine their textural characteristics (e.g., micropore volume, total pore volume pore, and external surface area), while scanning electron microscopy (SEM) was applied to visualize the shape and size of the zeolite particles. The coordination state of the incorporated Ti and Sn sites was studied using UV-vis spectroscopy, while FTIR spectroscopy of adsorbed base probe molecules (pyridine, 2,6-ditertbutylpyridine, d_3-acetonitrile) provided information on the nature and concentration of acid sites that are accessible to base molecules of different sizes. The results reveal that variation in the Si/Ge ratio allows one to modify the size and shape of IWW crystals as well as the concentration of acid sites incorporated into IWW and ITH zeolites.

Abstrakt

Tato bakalářská práce je zaměřena na syntézu, postsyntetickou modifikaci a komplexní charakterizaci dvou zeolitů založených na topologiích IWW a ITH. Zkoumané zeolity byly vybrány protože jejich struktury obsahují jednotky d4r přednostně obsazené Ge. Atomy Ge lze post-syntézní degermanací/metalací nahradit různými katalyticky aktivními kovy jako jsou Al, Ti a Sn.

Pro studium vlivu chemického složení výchozího germanosilikátu na koncentraci a přístupnost nahrazených kovových míst byly zeolity IWW a ITH hydrotermálně syntetizovány s různým množstvím germania v reakční směsi (Si/Ge = 4 – 10 pro IWW a Si/Ge = 10 – 30 pro ITH) a použity pro postsyntetické nahrazení Ge jiným kovem.

Připravené zeolity byly charakterizovány pomocí rentgenové difrakce (XRD), chemické analýzy, fyzisorpce dusíku, skenovací elektronové mikroskopie (SEM), infračervené spektroskopie s Fourierovou transformací (FTIR) a ultrafialové viditelné spektroskopie (UV-VIS). XRD potvrdila strukturu syntetizovaných zeolitů; chemická analýza identifikovala jejich prvkové složení; fyzisorpce dusíku určila jejich texturní charakteristiky (např., objem mikropórů, celkový objem pórů a vnější povrch), zatímco SEM zviditelnila tvar a velikost částic zeolitů. Koordinační stav inkorporovaných míst Ti a Sn byl studován pomocí UV-VIS spektroskopie, zatímco FTIR spektroskopie adsorbovaných testovacích molekul (pyridin, 2,6-ditertbutylpyridin, d_3-acetonitril) poskytla informace o povaze a koncentraci kyselých míst, která jsou přístupná pro molekuly bazí různých velikostí.

Table of contents

List of abbreviations

Abbreviation	Full name
ADOR	Assembly – Disassembly – Organization – Reassembly
BAS	Brønsted acid sites
BET method	Brunauer–Emmett–Teller method
d3r	double-3-ring
d4r	double-4-ring
ESI-MS	electrospray ionization mass spectrometry
FTIR	Fourier-transform infrared spectroscopy
HM(OH)$_2$	hexamethonium dihydroxide
ICP-MS	inductively coupled plasma mass spectrometry
IR	infrared spectroscopy
IUPAC	International Union of Pure and Applied Chemistry
IZA-SC	International Zeolite Association Structural Comission
LAS	Lewis acid sites
MPP(OH)$_2$	1,5-bis-(methylpyrrolidinium)-pentane
NMR	nuclear magnetic resonance
s4r	single-4-ring
SDA	structure directing agent
SEM	scanning electron microscopy
TEOS	tetraethyl orthosilicate
UV-vis	ultraviolet-visible
XRD	X-ray diffraction

1. Introduction

Zeolites are hydrothermally synthesized crystalline microporous aluminosilicates with broad applications in adsorption and catalysis. Zeolites contain micropores and acid (active) sites in the framework. In particular, active sites can be represented by metal atoms such as aluminium, titanium, and tin incorporated into a silica framework.[1]

From a structural point of view, zeolites consist of various building units.[2] Specifically, germanosilicates as a separated class of zeolites often contain double-4-ring (d4r) units in their frameworks.[3] In contrast to other elements, germanium atoms show limited catalytic potential but a unique preferential location in small cubic units of a zeolite framework, especially at high Si/Ge ratios.[4] This property of germanosilicate zeolites, together with the hydrolytic instability of Ge-O bonds[5] can be used to regulate the characteristics of catalyst and adsorbents through incorporation of active metal sites into specific T-positions of a framework (d4r units) originally occupied by germanium *via* the degermanation/metallation approach.[3]

2. Goals of the thesis

The aim of this B.Sc. thesis is to address whether and how the chemical composition of parent germanosilicate zeolite influences the physicochemical properties of Al-, Ti-, and Sn-substituted zeolites prepared by degermanation/metallation.

To achieve this general goal, the following tasks were solved in this study:

1) To synthesize IWW and ITH germanosilicates with different concentrations of Ge in the framework;

2) To incorporate Al, Ti, and Sn atoms into the frameworks of prepared zeolites by post-synthesis Ge-for-metal substitution;

3) To characterize the physicochemical properties of prepared zeolites using X-ray diffraction (XRD), chemical analysis, nitrogen physisorption, scanning electron microscopy (SEM), Fourier-transform infrared (FTIR) spectroscopy, and ultraviolet-visible spectroscopy (UV-vis) spectroscopy.

3. Theoretical part

3.1. Zeolites

Zeolites are crystalline microporous materials with three-dimensional structures and versatile chemical compositions. Although only aluminosilicate zeolites are formed in nature, synthetic zeolites can contain different three- and four-valent elements in the silica matrix. These elements are, for example, boron, iron, gallium, titanium, tin, zirconium, hafnium, and germanium.[6]

The intrinsic properties of zeolites determine their broad applications. For example, due to the negative charge of the framework, aluminosilicate zeolites have ion-exchange ability, which is used in washing powders to remove Ca^{2+} and Mg^{2+} ions from water. The presence of three-valent or some four-valent elements (see Section 3.1.2) gives rise to the acidity of zeolites, which is used to catalyse some of the industrially important reactions. Specifically, zeolite catalysts play an important role in many industrial processes, such as isomerization, alkylation, and catalytic cracking. In addition, due to the uniform and high porosity, zeolites are used as industrial adsorbents. Examples of such an application are separation of gas mixtures, removal of harmful compounds from water and gases, etc.[7]

Today, more than 250 structural types of zeolites are known.[2] However, the number of synthesised zeolites is remarkably lower compared to the number of hypothetical zeolite structures.[8]

3.1.1. History

The first mention of a zeolite was in 1756. During the investigation of probably stilbite, a Swedish mineralogist, Axel Fredrik Cronstedt, discovered that water steam is released if this natural zeolite was exposed to flame. The detected reverse adsorption of water is one of the features of zeolites, from which the name zeolite came. In fact, *zeolite* is the connection of two Greek words, *zeo* = "to boil" and *lithos* = "stone".[1]

In the 1940s, zeolites were used in industry as adsorbents. In 1959 zeolites were applied for the first time as industrial catalysts in fluid catalytic cracking.[9] Currently, the main use of zeolites is in catalysis (the crude oil industry), selective adsorption, and ion exchange. However, scientists are focused on the synthesis of new zeolite structures and the optimisation of existing ones because of the high potential of zeolite catalysts for new processes in the chemical industry.

3.1.2. Structural properties

The elementary unit of a zeolite framework is a tetrahedron. The tetrahedron is formed by a central T element (for example, Si^{4+}, Al^{3+}, Ge^{4+} and Ti^{4+}) and four oxygens. Tetrahedra are connected through shared oxygen corners into more complex secondary building units, the connection of which forms a final zeolite framework (Figure 1).[1] The variability of the connections of tetrahedra, which results in different complex building units, is the reason why so many different types of zeolites (> 250 already known zeolites and > 1,000,000 predicted zeolite structures) can be constructed using the same type of tetrahedra.[8]
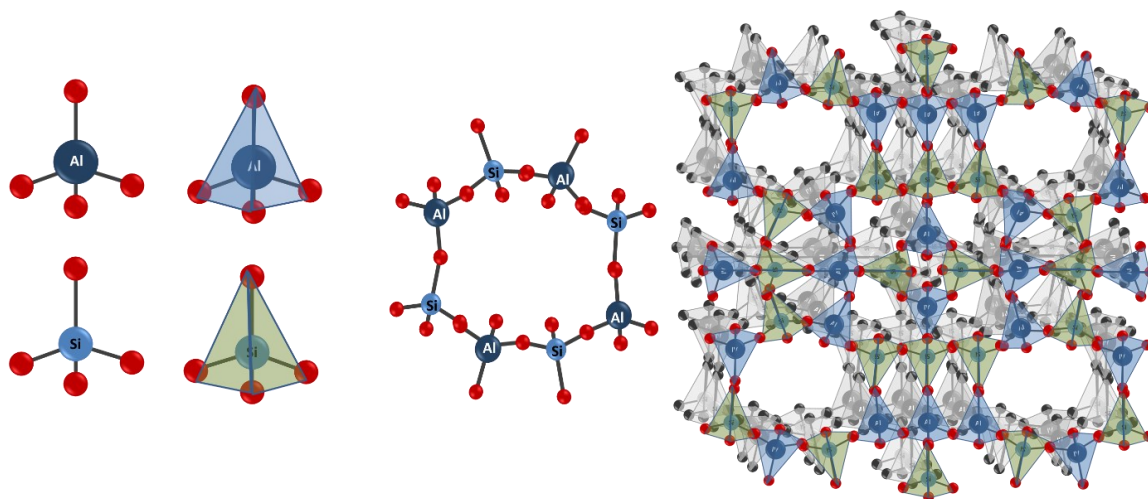
Figure 1: Silica and alumina tetrahedra connected in a zeolite framework (red balls illustrate oxygen atoms)[10]

The channels (and cavities) within the native structure of a zeolite are shown in Figure 1. These channels have a precisely defined shape and size, ranging from 3 to 12 Å. The size of zeolite channels defines which molecules can pass through the pore system of a zeolite adsorbent or catalyst and, as a result, is decisive for its application in a specific process. The uniform porosity of zeolites provides 1) a molecular sieving effect used in adsorption and separation and 2) shape selectivity used in separation and catalysis. Zeolites are classified into four groups according to pore sizes: small, medium, large, and extra-large pore zeolites (Table 1).[1]

Table 1: Classification of zeolites according to micropore size

Classification	Number of tetrahedra limiting a channel entrance	Approximate Pore diameter (Å)
Small pore	8	< 4
Medium pore	10	< 5.5
Large pore	12	< 7.5
Extra-large pore	> 12	> 7.5

According to their chemical composition, the aluminosilicate zeolites are classified into low-silica (molar ratio of Si/Al < 10) and high-silica (Si/Al > 10).[3] The negative charge of the aluminosilicate zeolite frameworks is given by the number of tetrahedrally coordinated Al^{3+} ions. In fact, the $[AlO_{4/2}]^{-1}$ tetrahedron in a zeolite framework holds charge -1, because each Al atom with oxidation state +3 is surrounded by 2 oxygen atoms (that is, 4 O atoms are shared between 2 tetrahedra) with an oxidation state -2. This negative charge is compensated by cations, both inorganic (mostly alkali and alkaline earth metals) and organic (typically tetraalkylammonium). Charge-compensating cations are located in the so-called cation-exchange positions. When a negative charge of the framework is compensated by protons, Brønsted acid sites (BAS) are formed.

According to the Brønsted and Lowry theory (1922-1923), Brønsted acid is a system, that is capable of donating a proton H^+.[11] In zeolites, Brønsted acid sites are formed by bridging hydroxyl groups (Figure 2), when three-valent elements T^{3+}, such as Al^{3+}, Ga^{3+}, and Fe^{3+} are incorporated into the silica framework.[6]
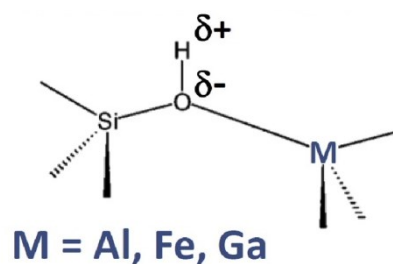
Figure 2: Brønsted acid site formed by incorporation of 3-valent elements in a zeolite[6]

Lewis acidity is also a characteristic feature of metallosilicate zeolites. Lewis theory (1923) describes an acid as a species (ion, molecule, substance) that has a free orbital to accept an electron pair from another species (Lewis base) forming an acid-base adduct.[11] In zeolites, Lewis acidity arises, in particular, due to the incorporation of tetravalent elements (usually Sn or Ti) into tetrahedral positions (Figure 3). As a result of coordinative unsaturation, such sites can form the adducts with Lewis bases (e.g., pyridine). On the other hand, dihydroxylation of the Brønsted acid sites (Figure 3) leads to Lewis acid sites (LAS), associated with coordinatively unsaturated Al.
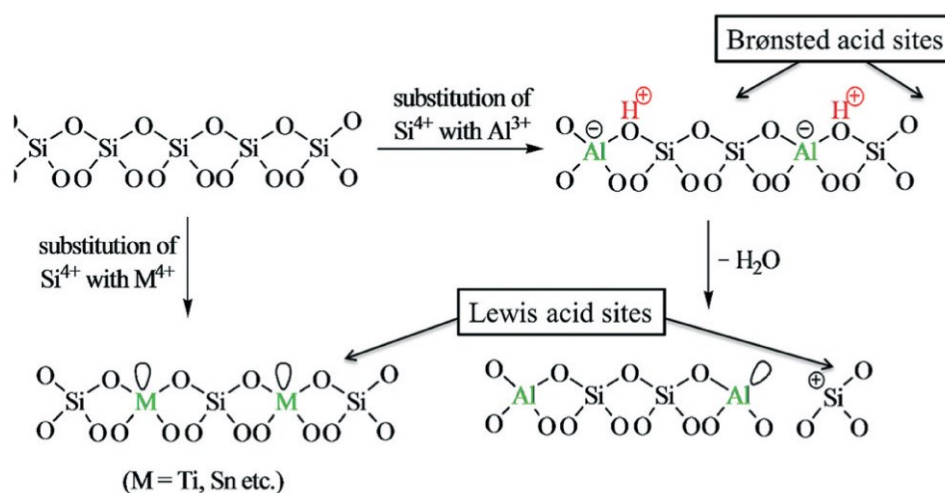
Figure 3: Brønsted and Lewis acid sites in zeolites[12]

3.1.3. Hydrothermal synthesis

Zeolites are prepared under hydrothermal conditions at temperatures in the range of 100 – 240 °C and pressures of up to 2 MPa. Due to such harsh conditions, vessels for zeolite synthesis must have high resistance to high temperatures and pressures. In practice, hydrothermal crystallization of zeolites is performed in autoclaves, which are sealed metal vessels into which sealed Teflon containers are inserted. For the maintenance of isothermal conditions, the oven is used.[13] Hydrothermal synthesis may be performed under static conditions or rotation of the autoclave with a reaction mixture.

The reaction mixture for the synthesis of zeolite usually contains the sources of 1) elements for the building of the framework (for example, Si, Al, Ge), 2) inorganic and/or organic cations as the structure-directing agent (SDA), 3) inorganic anions to control pH facilitating crystallization (hydroxyl or fluoride anions) and solvent, typically water.[13]

The crystallization of zeolites includes several steps. In the first step, which is called an induction period, the individual components are mixed together, and an intermediate

(noncrystalline) solid phase is formed prior to the appearance of an ordered zeolite structure. In the second nucleation step, small (~ 10 nm) zeolite crystals are formed[14]. Finally, during the crystal growth step, larger zeolite crystals are evolved (usually larger than 50 nm).[1,14]

Tetraethyl orthosilicate (TEOS), fumed silica, colloidal silica sol, and sodium water glass are the most used sources of Si. Chlorides or alkoxides can be used as sources of Al, Ti, and Sn, while germanium oxide is typically applied as a source of Ge. These raw materials have different reactivity and solubility. As a result, they affect the crystal size and crystallization rate of a specific zeolite. The ratios of the individual components of the mixture are important for the formation of zeolites. These ratios influence the chemical composition and structure of the formed zeolite.[13]

Organic SDAs (templates) are ions or neutral molecules that affect the growth of a specific structure of zeolite by stabilizing a zeolite framework *via* Coulombic and van der Waals interactions. The addition of SDA to the synthesis mixture facilitates crystallization of a particular zeolite framework, which would not arise without this organic template. However, one type of zeolite can arise from several types of organic SDA, and one template can be used for the synthesis of several types of zeolites. Generally, if an aluminosilicate zeolite can be formed either in organic-free or organic-containing reaction mixtures, the presence of organic templates favours the crystallization of a zeolite with higher Si/Al ratios.[1]

In hydrothermal synthesis, water acts not only as a solvent but also as the reaction component, which interacts with the low-molecular reactants and polymeric (framework) intermediates or products. Adding more water usually decreases the concentration and therefore the number of nucleation centers, causing larger crystals in the final product.[13]

Crystallization time and temperature are very important parameters because zeolites crystallize as metastable phases. This means that the synthesis of a certain type of zeolite can only be achieved at a certain range of temperatures and within a certain range of crystallisation time. If this time or temperature is not used, other phases, usually amorphous or other types of zeolites, can be formed or the synthesis does not proceed at all.

Stirring during crystallization may facilitate the formation of a zeolite. By mixing, a larger number of crystallization centers can be achieved as a result of the faster saturation of the solution. In addition, seeding makes the synthesis faster and more selective. It can be done by adding a small amount of synthesised zeolite to a reaction mixture.[15]

In my work, hydrothermal crystallization was used for the synthesis of two germanosilicate zeolites, IWW and ITH. The pure phase of ITH zeolite can be synthesized with a Si/Ge ratio from 4.8 to infinity using hexamethonium dihydroxide as an SDA.[16] On the other hand, IWW formation has been reported in the narrower ranges of Si/Ge ratios 1.0 – 6.6 using 1,5-bis-(methylpyrrolidinium)-pentane as an SDA.[17,18] In my study, the seeding approach was attempted to enlarge the range limits of the Si/Ge ratios for the IWW crystallization.

3.2. Germanosilicate zeolites

Ge was incorporated into the frameworks of many zeolites and also gave rise to previously unknown zeolite structures, first discovered in germanosilicate systems. Germanium is the element closest to silicon in terms of chemical properties. For example, GeO_2, like SiO_2, crystallizes with the formation of quartz and rutile structures.[19,20] On the other hand, germanium is significantly different from silicon in some properties. For example, the length of the Si–O

14

bond for 4-coordinated silicon is usually within 1.60 - 1.63, while the Ge–O bond length is in the range of 1.70 to 1.80 Å.[21] The T–O–T angles in germanates are usually much smaller (117 – 145°) than in silicates (135 – 180°).[21,22] Thanks to the mentioned properties, the incorporation of Ge into zeolites facilitates the creation of small cubic d4r units consisting of 8 tetrahedra with Si or Ge T-atoms.[23,24]

Specifically, the IWW and ITH germanosilicate zeolites studied in this work contain d4r units in their frameworks (Figure 4). IWW has a pore system with 12-10-8-ring channels, while ITH has 10-10-9-ring channels in the structure.
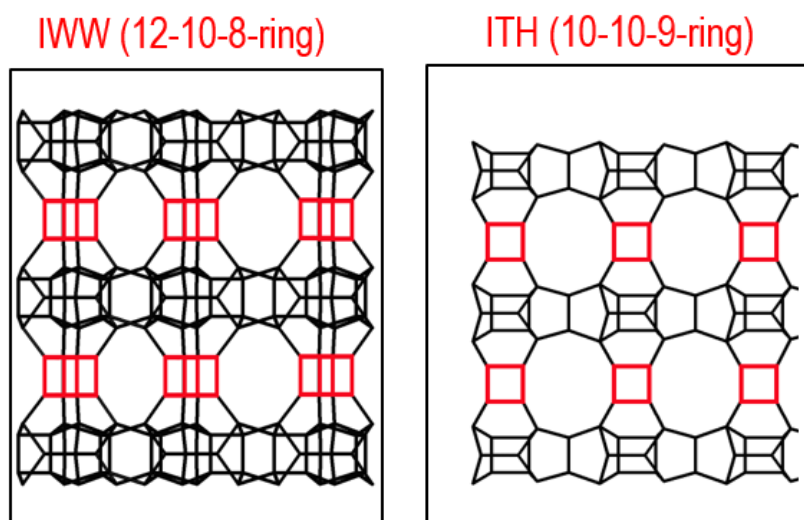

Figure 4: Structures of the IWW and ITH zeolites (d4r units are shown in red).

Using the ESI-MS method, it was found that cubic $Ge_8O_n^{-(2n-32)}$ species resembling d4r units have already formed in germanosilicate reaction mixtures after mixing the reagents before the crystallisation of zeolite started.[24] Theoretical calculations and calorimetric measurements revealed a decrease in the thermodynamic stability of silica zeolites (the enthalpy of crystallization), when Ge is inserted into the framework.[25] Therefore, the favorable formation of d4r-containing zeolites in the presence of Ge is related to the shift of the equilibrium concentration toward cubic $Ge_8O_n^{-(2n-32)}$ species in the reaction mixture. Favoring the formation of double-3-ring (d3r) and d4r units in zeolites, Ge atoms favorably fill the positions in those small units.[4,18,26]

The location of Ge in d4r units of UTL zeolite combined with the hydrolytic instability of the Ge–O bonds was used to synthesize new zeolites. This method is called ADOR (abbreviation of Assembly – Disassembly – Organization – Reassembly, Figure 5).[27] The first step of ADOR is Assembly. It corresponds to the synthesis of parent zeolites with preferential location of Ge atoms in d4r units. In the next Disassembly step, germanium and silicon atoms are removed from d4r units due to the selective degradation of Ge– O(Si)/Ge– O(Ge) bonds by water, while the crystalline silica layers preserve their structure. In the third Organization step, the arrangement of silica layers in a special manner with respect to each other is provoked by changing the treatment conditions. Finally, in the last Reassembly step, condensation of the layers leads to a new zeolite framework; its structure differs from the initial one due to the modification of the interlayer units. For example, the layers in formed zeolites can be connected by oxygen bridges, d4r or single-4-ring (s4r) units, or a combination of units of several types.

The type of connection in the final zeolite determines the size of the pores and thereby the textural properties of the material.[3]
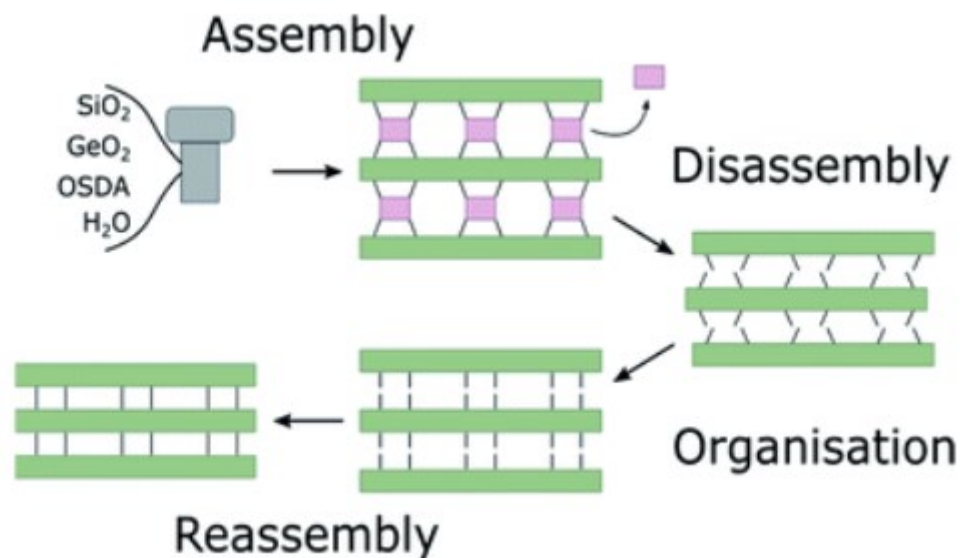
To prepare catalytically active zeolites, the ADOR method was combined with the incorporation of metal sites in either the Assembly (shown for Al [29] and Ti [30]) or Disassembly (shown for Al [31]) step. One of the benefits of the ADOR technique is that it opened the way to the sets of zeolite catalysts with similar layers within the structure but different micropore sizes (Figure 6).

Active sites can also be incorporated into germanosilicate zeolites without structural modification by direct hydrothermal crystallization or post-synthesis substitution of Ge for the desired metal (e.g., Al, Ti, Sn). There are three reasons why post-synthesis Ge-for-metal substitution is favourable compared to hydrothermal crystallization: 1) post-synthesis enables higher metal loading into specific zeolite framework[32], 2) it permits recycling and reuse of germanium, which enables cost reduction for overall synthesis,[33] and, finally, 3) it may provide control over positioning of incorporated metal atoms at certain sites of the framework. The post- synthesis isomorphous substitution was achieved by two-step degermanation/metallation of Ge-poor materials (Figure 7).[6] The first step is the creation of "silanol nests" by degermanation. Further metallation is applied for the introduction of heteroatoms and the modification of the nature of acid sites in a zeolite for specific application. "Ge-poor" is a qualitative characteristic that refers to the structural stability of a zeolite under hydrolysis conditions. For example, the IWW zeolite structure was found to be stable when the Si/Ge molar ratio is 6 but its framework is destroyed when Si/Ge is < 3. And the ITH zeolite structure was found to be stable when the Si/Ge molar ratio is 10 but its framework is destroyed when Si/Ge is < 2.[5]
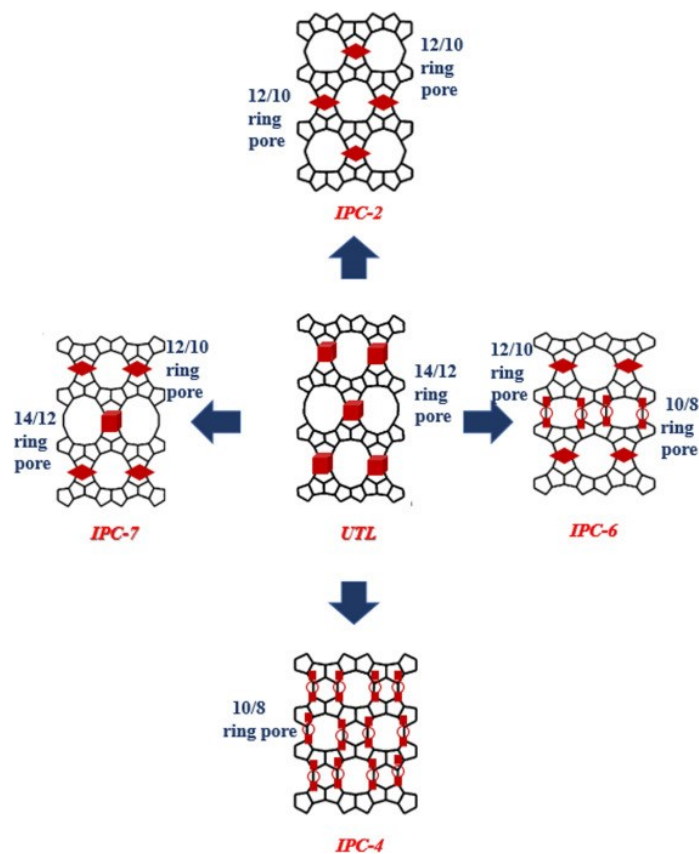
Figure 6: Al- and Ti-substituted zeolite catalysts prepared by a combination of ADOR and metal incorporation into UTL germanosilicate.[30]
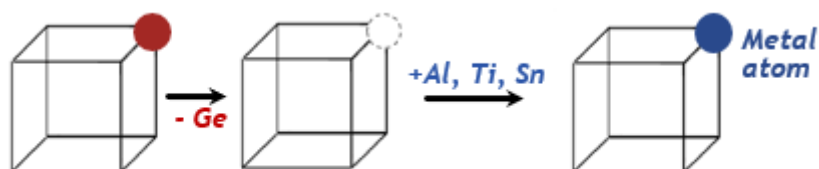
Figure 7: Scheme of degermanation/metallation. The cubes show d4r units, the red point is germanium, and the blue point shows a metal atom (Al, Ti, Sn). In the first step, Ge is removed from the structure, whereas in the second step, the formed vacancy is filled by another metal atom.

Thus, post-synthesis modification of germanosilicate zeolites allows to synthesize zeolites with new structures, chemical compositions, and, likely, a controllable location of metal sites.

3.3. Characterization of zeolites

A range of possible applications of zeolites requires their thorough characterization to determine specific properties (structure, porosity, acidity, crystal size, and shape, among others), which improve an outcome of a particular process. The structural identification of a zeolite is based on diffraction methods, such as X-ray diffraction (XRD, Section 3.3.1). The size and shape of the zeolite crystals are determined using scanning electron microscopy (Section 3.3.2). The textural properties of zeolites (e.g., pore volume and surface area) are evaluated using nitrogen physisorption (Section 3.3.3). Spectroscopic methods, such as UV-vis

and FTIR spectroscopies based on the interaction of matter with electromagnetic radiation (Figure 8) are used for the characterization of the type and strength of acid sites in zeolites and the coordination of metal sites (Section 3.3.4).
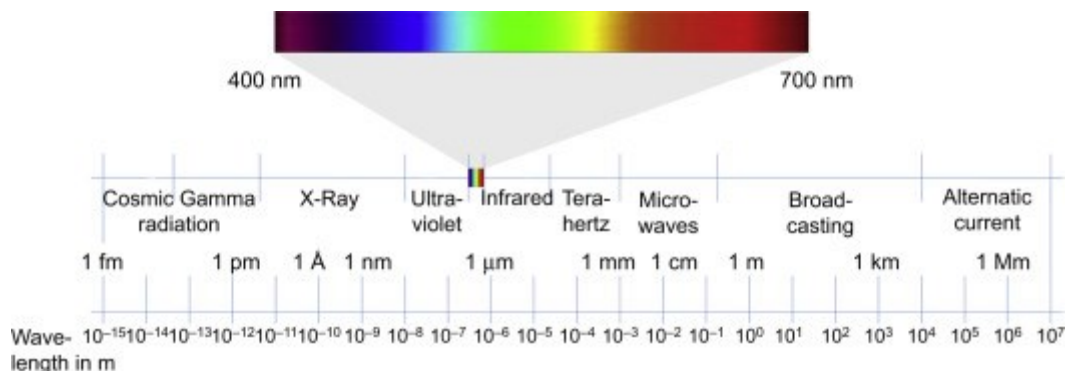
Figure 8: The spectrum of electromagnetic radiation[34]

3.3.1. X-ray diffraction

X-ray diffraction is the characterization method used for the study of the structural properties of zeolites. In particular, it is used to verify the structural type of the synthesised zeolite, its phase purity, and crystallinity. XRD is the method, which also helps to detect the new zeolite structures and determine their unit cell type and size.

The repeating arrangement of atoms in a crystal forms a lattice with well-defined repeating distances. As the wavelength of the X-rays is in the same range as the spacing of atoms in a zeolite (Figure 9)[35], the interference of the X-rays scattered from a zeolite may occur and results in the appearance of a diffraction pattern with regions of higher and lower intensities. The amplification or constructive interference of the produced signal occurs at particular angles determined by the Bragg equation (Figure 9). For monochromatic X-ray radiation with a wavelength λ, the maxima in the diffraction pattern meet the following condition:

$$n\lambda = 2d\sin\theta$$

where

n is the integer number (diffraction order);
λ is the wavelength of the X-rays;
d is the distance between the atomic planes (Figure 9);
θ is the angle between the incident rays and the diffracting planes (Figure 9).[36]

Figure 9: Bragg's law for two-dimensional crystal[37]

18

The zeolite sample is usually measured over a wide range of θ angles to achieve all possible diffraction directions. Calculating the d-spacings between the atomic planes based on Bragg's law allows one to identify univocally the zeolite structure because each type of zeo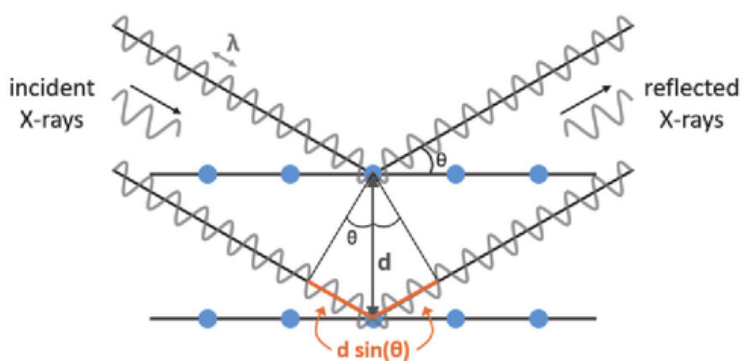lite structure has a set of unique d-spacings. For this, the positions of the diffraction lines and their intensities in the sample of interest are compared with the diffraction patterns in a database of known zeolite structures. If identical plots (in terms of positions) cannot be found, the probable outcome of a synthesis is a mixture of two or more types of zeolites or a new zeolite.[36]

In powder X-ray diffraction, a sample consisting of a large number of small crystals is irradiated by X-rays. Because the crystals are situated randomly in relation to the X-ray source, the phenomenon of preferential crystal orientation may affect the relative intensities of the diffraction lines and complicate the solution of the new zeolite structures. To avoid this phenomenon, a thorough grinding of the zeolite sample is done before the measurement.

3.3.2. Scanning electron microscopy

Scanning electron microscopy (SEM) makes possible the visualization of zeolite crystals. The resolution power of optical microscopy is often not enough to image small zeolite crystals. The reason is the too high wavelength of visible light (380 – 780 nm, Figure 8), which does not allow one to achieve a resolution better than 200 nm. Unlike an optical microscope, electron microscopes rely on the interaction of matter with electron beams accelerated by the electric field and focused using electromagnetic lenses instead of glass optics (Figure 10). According to Louis de Broglie, electrons are similar to light in the sense that they propagate like waves. The wavelength of the electrons, λ, is much lower compared to visible light and depends on the accelerating voltage (e.g., ~40 pm for 1 eV, ~12 pm for 10 eV, ~4 pm for 100 eV).
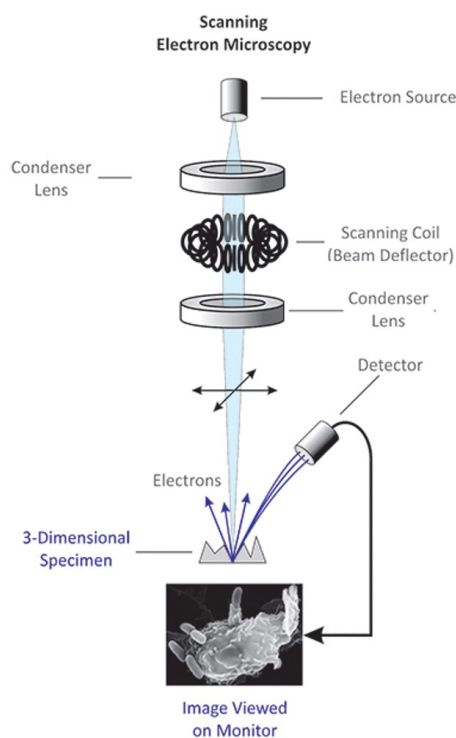

Figure 10: Principle components of the scanning electron microscope.[38]

Thus, the resolving power of an electron microscope is several orders of magnitude higher than that of the optical microscope. Practically, the resolution of SEMs is often limited to 1 – 10 nm, depending on several factors, such as the type of electron gun (thermionic emission or field emission), the physical limitations of the electromagnetic lens system that forms the probe, and finally the specimen itself.[39]

3.3.3. Physisorption

Studying the porosity of zeolites (volume and size of the pores, surface area) is based on the physisorption phenomenon, that is, the enrichment of the surface of a solid material (adsorbent) with gas or liquid (adsorbate).[40] In the physisorption process, van der Waals forces between the adsorbent and the adsorbate attract adsorbate molecules to the surface of a solid. The same process occurs in porous materials and can be used for the characterization of their porosity. Taking into account the International Union of Pure and Applied Chemistry (IUPAC) classification, pores in nanomaterials can be distinguished according to their sizes: 1) micropores (diameter < 2 nm); 2) mesopores (2 – 50 nm), and 3) macropores (> 50 nm). Micropores exist in the inner part of zeolite crystals.[40]

Nitrogen is the most widely used adsorbate for the physisorption studies of zeolites. The reason is that nitrogen is a practically nonreactive gas and is available at a good price. With the help of nitrogen physisorption, the micropore volume and total pore volume as well as the surface area of the zeolites can be determined. In turn, for the micropore size analysis, more inert argon is the adsorbate of choice.[41] The specific reason for that is that argon does not exhibit a specific interaction with functional groups on the surface of the measured material. This is important for the accurate determination of the micropore sizes of materials, such as zeolites, some oxides, and active carbon and metal organic frameworks. Information on porosity is gained from analysis of the adsorption isotherm, which shows the volume of adsorbed gas against its relative pressure under isothermal conditions (that is, -195.8 °C, the boiling point of nitrogen). The shape of the isotherm depends on the pore system in a material and on the features of adsorbate-adsorbent interactions. According to the IUPAC classification, there exist eight types of isotherms (Figure 11).

Type I adsorption isotherms, I(a) and I(b), have a characteristic pattern, that is, the adsorbed amount increases rapidly up to the limit value at quite low $p/p_0 < 0.1$. Such shapes of adsorption isotherms are typical for zeolite materials. Materials with small micropores (< 1nm) show a nitrogen adsorption isotherm of type I(a) where maximum adsorption (plateau in adsorption isotherm) is reached at relatively low p/p_0 (< 0.03), while those with larger micropores (~2nm) show N_2 adsorption isotherms of type I(b) which reaches the maximum adsorbed value at higher p/p_0 (< 0.1).

The Type II adsorption isotherm is characteristic of nonporous or macroporous adsorbents (but these cannot be specified by analysis of the isotherm shape). The Type II isotherm consists of three parts: 1) concave-shaped, 2) linearly progressing; 3) convex-shaped. At the point where the concave part transitions to the linear part, the multilayers of adsorbed molecules start to form, so this point provides information on the p/p_0 value corresponding to the completed monolayer.

The Type III adsorption isotherm is typical of a weak adsorbate-adsorbent interactions (e.g., water vapours adsorbed on hydrophobic material); it has a convex shape in the entire range of $0 < p/p_0 < 1$.

Similarly, to the type II adsorption isotherm, type IV adsorption isotherm has 3 parts, corresponding to the formation of adsorbent monolayer, multilayer and finally capillary condensation. This type of adsorption isotherm is typical for mesoporous materials. Type IV isotherms are divided into type IV(a) and type IV(b). The IV(a) type isotherm has a hysteresis loop, created by a mismatch of p/p_0 at which the pores are filled and released by an adsorbate during the adsorption and desorption steps. During the adsorption step, the pores are filled at pressures that depend on the pore size. Emptying the pores during desorption also depends on their size and takes place at lower pressures compared to the pressure at which the pores are filled. The type IV(b) isotherm follows the same pattern as the type IV(a) isotherm, with the only difference that there is no hysteresis loop in the type IV(b) isotherm, that is, adsorption and desorption take place at the same pressure values.
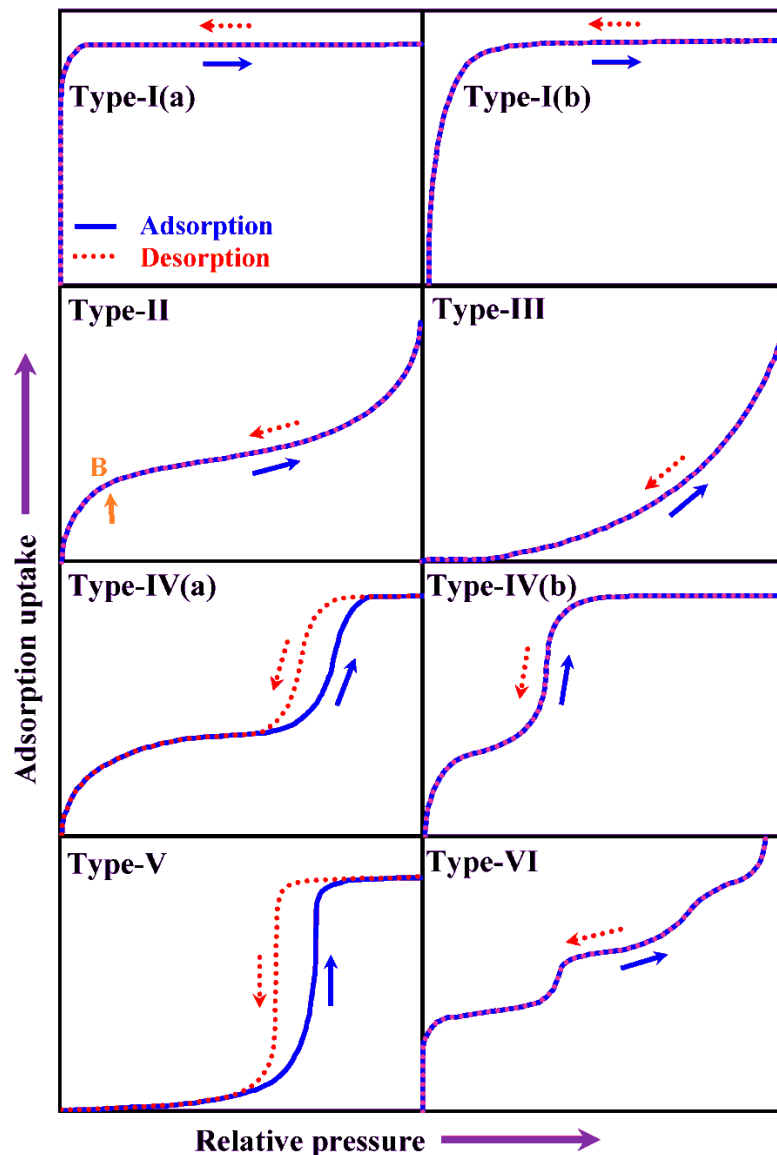

Figure 11: Types of adsorption (desorption) isoterms [42] Adsorption branches are shown in blue, and desorption branches are shown in red.

The Type V isotherm shows a convex shape at low pressure and saturation at high pressures. This type of isotherm is typical for weakly interacting adsorbate-adsorbent pairs and shows the presence of a hysteresis loop upon adsorption/desorption in the pores.

Type VI is a multi- step isotherm that is relatively rare and occurs in materials that have a uniform surface.

The total adsorption volume is usually measured at the relative pressure $p/p_0 = 0.95$ from the adsorption branch of the isotherm. The volume of micropores is determined using the t-method of de Boer and Lippens.[43] According to this method, a dependence of the adsorption volume on the thickness of the adsorption layer (t) must be plotted for the studied sample. For that purpose, an adsorption isotherm of a standard non-porous sample, such as a silica gel, is measured and the thickness of the adsorption layer is calculated at different p/p_0 as

$$t = V_{ads}/S$$

where

V_{ads} is the adsorbed volume at specific p/p_0;
S is a specific surface area of the standard sample.

Using the dependence $t - p/p_0$ for a standard material, the sample adsorption isotherm of the studied is constructed in the coordinates $V_{ads} - t$:

$$V_{ads} = V_{micro} + S_{ext}t$$

The volume is then found as the intercept of the $V_{ads} - t$ curve in the range $t = 0.3 - 0.45$, while the slope of the curve in the range $t = 0.6 - 1$ nm gives the specific external surface of the sample, S_{ext}.

3.3.4. Spectroscopy

Spectroscopic techniques, such as IR and UV-vis spectroscopies, detect the absorption of electromagnetic energy after it illuminates the sample. Depending on the chemical composition, zeolite absorbs radiation of a particular wavelength, which corresponds to the energy required for the transition from one state (electronic or vibrational levels) to another. This allows qualitative analysis of the absorbing species in zeolite materials (e.g., 4- and 6-coordinated Ti atoms in zeolites using UV-vis spectroscopy). On the other hand, the amount of absorbed radiation depends on the number of such species, which allows for quantitative analysis using the Beer-Lambert law:

$$\log\frac{I_0}{I} = A = \varepsilon \cdot l \cdot c$$

where

I_0 and I are the intensities of incident and transmitted radiation, respectively;
A is absorbance;
ε is molar absorption coefficient;
l is path length of the beam;
c is concentration of absorbing species.[36,44]

The absorption of infrared radiation results in transitions between vibrational levels. The absorption of visible and ultraviolet radiation results in transitions between electronic energy

levels. The result of spectroscopic measurements is represented as a spectrum that shows the dependence of transmitted (or absorbed) light on the wavelength. For example, the transmittance mode of IR spectroscopy, that is, the detection of light passed through a thin self-supported wafer of a material, is usually used to analyse the concentration and type of acid sites in zeolites.

3.3.4.1. IR spectroscopy

The range of electromagnetic spectrum for infrared spectroscopy is 12000 to 10 cm^{-1}. This range is divided into three specific regions, corresponding to far-infrared (smaller than 400 cm^{-1}), middle-infrared (4000 – 400 cm-1), and near-infrared (12000 – 4000 cm^{-1}).[45] Mid-IR spectroscopy is usually used to characterise zeolites.

In the framework vibration region (1500 – 200 cm^{-1}), two types of T-O vibrations are observed. The first group of bands that refer to the vibrations of the T-O bonds within tetrahedra is structurally insensitive and includes asymmetric (950 – 1250 cm^{-1}) and symmetric (650 – 720 cm^{-1}) T-O stretching vibrations and bending O-T-O vibrations (420 – 500 cm^{-1}). The second group includes inter-tetrahedra structure-sensitive vibrations assigned to double rings (500 – 650 cm^{-1}), symmetric stretching (750 – 820 cm^{-1}) and asymmetric stretching (1050 – 1150 cm^{-1}). The vibrations of the zeolite framework can be used to investigate the isomorphic incorporation of some elements (e.g., B and Ti) into the zeolite framework. This incorporation is most commonly detected by the appearance of characteristic bands in the 1500 – 850 cm^{-1} region (e.g., 1380 and 920 – 890 cm^{-1} for B and 960 cm^{-1} for Ti).

The stretching vibrations of the OH groups characteristically occur in the region 3800 – 3200 cm^{-1}.[46] Bridging OH groups of Brønsted-type acid sites are observed in the range 3650 – 3600 cm^{-1} (for example, ~3610 cm^{-1} for Al-substituted zeolites, ~3620 cm^{-1} for Ga-substituted zeolites, ~3625 cm^{-1} for Fe-substituted zeolites).[47,48] Furthermore, silanol groups on the outer surface of zeolite crystals are detected in the range of 3740 – 3745 cm^{-1}, while the vibration of "internal" silanols corresponding to structural defects is shifted to the range of 3735 - 3715 cm^{-1}.

Organic bases with different strengths (for example, ammonia, amines, carbon monoxide) are used as probe molecules to distinguish the type and strength of acid sites in zeolites. Pyridine is the most widely used probe molecule. After the adsorption of pyridine in zeolite, we obtain a new spectrum, from which we can calculate the concentrations of the Brønsted and Lewis acid sites (Figure 12). The bands corresponding to Brønsted (1545 cm^{-1}) and Lewis (1454 cm^{-1}) acid sites are well separated in IR spectra of adsorbed pyridine.[46] The intensities of the respective bands are used for the evaluation of the number of corresponding acid sites using Lambert-Beer law.
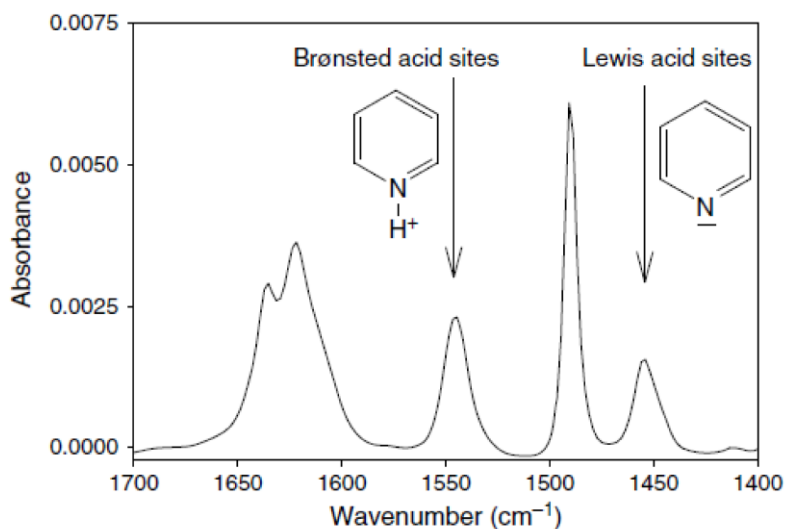
Figure 12: The FTIR spectrum of pyridine adsorbed in a zeolite shows the characteristic bands of the Brønsted and Lewis acid sites[49]

d₃-acetonitrile is another probe molecule frequently used for detection and evaluation of different acid sites in zeolites. The advantage of d₃-acetonitrile is its smaller kinetic diameter (0.4 nm), which allows the detection of acid centers in small-pore zeolites. However, the absorption bands corresponding to the interaction of d₃-acetonitrile with acid sites of different type and strength usually overlap. For example, adsorption of d₃-acetonitrile in aluminosilicate zeolites gives rise to several absorption bands (Figure 13): 2297 cm⁻¹ (characteristic for strong Al Brønsted acid sites), 2315 cm⁻¹ (weak Al Lewis acid sites) and 2325 cm⁻¹ (strong Al Lewis acid sites). The Ti and Sn Lewis acid sites show the bands at 2304 cm⁻¹ and 2310 cm⁻¹ in the IR spectrum of adsorbed d₃-acetonitrile.[50,51]
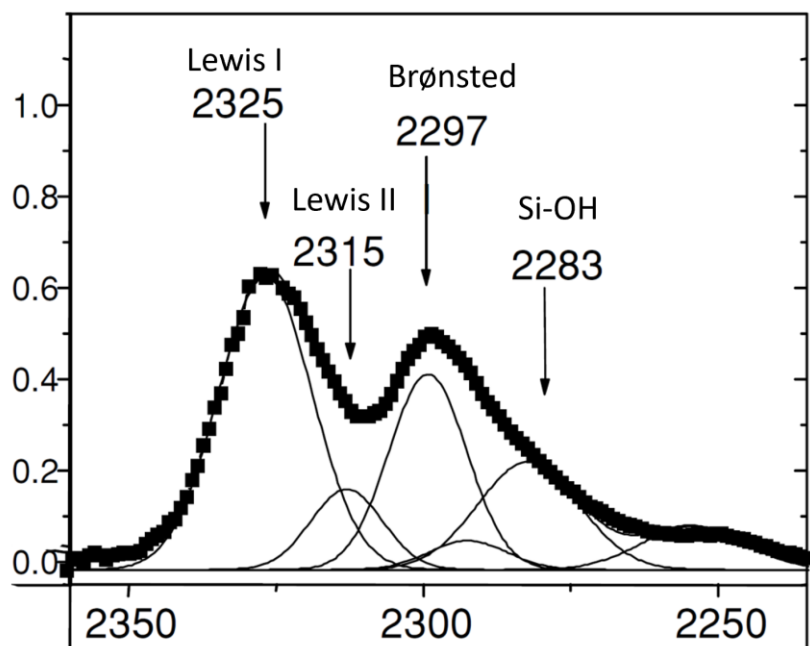
Figure 13: The FTIR spectrum of d₃-acetonitrile adsorbed in aluminosilicate zeolite shows the characteristic bands of the Brønsted and Lewis acid sites[52]

3.3.4.2. UV-vis spectroscopy

UV-vis spectroscopy uses the radiation in the UV range (200 – 800 nm) and visible range (380 – 780 nm) of the electromagnetic radiation spectrum. In the UV range, we can distinguish three subregions: UV-C (200 – 290 nm) UV-B (290 – 320 nm), and UV-A (320 – 400 nm).[28]

In the case of zeolites, UV-vis spectroscopy is used to study the incorporation of some 4-valent elements into the zeolite framework. For example, Ti, Zr, and Sn tetrahedrally coordinated by oxygens in the zeolite framework give rise to absorption bands at ~230 [54], ~215 [55] and ~210 [56] nm, respectively. On the contrary, the same elements in the extra-framework positions absorb at ~265 (Ti) [54], ~250 (Zr) [55], ~240 nm (Sn). [56] As the transitions between electronic levels involve different vibrational levels available for each electronic level, the absorption bands in the UV-vis spectra are much broader than those observed in the IR spectra.

4. Experimental part

4.1. List of used chemicals

Table 2: List of chemicals used

Chemical	Purity	Dealer
1,5-dibromopentane	97 %	Sigma Aldrich
2,6-ditertbutylpyridine	≥97%	Sigma Aldrich
Acetone	≥97%	Sigma Aldrich
Aluminum nitrate nonahydrate	≥98%	Sigma Aldrich
Ambersep® 900(OH)	-	Sigma Aldrich
d_3-acetonitrile	100%	Sigma Aldrich
Ethanol, ISO reagent	99.8%	Lachner
Germanium oxide	99.9%	Alfa Aesar
Heptane anhydrous	99%	Sigma Aldrich
Hexamethonium dibromide	≥98%	Sigma Aldrich
Hydrochloric acid	37%	Sigma Aldrich
Hydrochloric acid (ANALPURE®)	34-37%	Sigma Aldrich
Hydrofluoric acid	50%	PENTA
Hydrofluoric acid (ANALPURE®)	47-51%	PENTA
Nitric acid (ANALPURE®)	67-69%	Lachner
N-methylpyrrolidine	97 %	Sigma Aldrich
Pyridine	≥99%	Sigma Aldrich
Quinoline	98%	Sigma Aldrich
Tetraethyl orthosilicate	100%	VWR Chemicals
Tin(IV) chloride solution, 1M in heptane	-	Sigma Aldrich
Titanium(IV) chloride solution, 1M in toluene	-	Sigma Aldrich
Toluene anhydrous	99.8%	Sigma Aldrich

4.2. Synthesis of organic SDAs

4.2.1. 1,5-bis-(methylpyrrolidinium)-pentane dihydroxide

1,5-bis-(methylpyrrolidinium)-pentane dihydroxide (MPP(OH)$_2$) was prepared according to [17] and used for the synthesis of IWW zeolite. First, N-methylpyrrolidine (10 g) was alkylated with 1,5-dibromopentane (9.4 g) in acetone (150 ml) for 24 hours under reflux. Then, the solid material, MPPBr$_2$, was isolated by filtration and washed with acetone to remove unreacted amine. Finally, MPPBr$_2$ was dissolved in water and mixed with a required amount of Ambersep® 900(OH) anion exchange resin (0.8 mmol of MPPBr$_2$ per 1 g of anion exchange resin) to replace ions of Br$^-$ with ions of OH$^-$. The MPP(OH)$_2$ aqueous solution was concentrated at 35 Torr and 30 °C until the hydroxide concentration was > 1.0 M (measured by titration with 0.01 M HCl using methyl red as indicator).

4.2.2. Hexamethonium dihydroxide

The SDA hexamethonium dihydroxide (HM(OH)$_2$) was prepared by dissolving hexamethonium dibromide in water and mixing the prepared solution with an appropriate

amount of Ambersep® 900(OH) anion exchange resin (0.8 mmol of $HMBr_2$ per 1 g of anion exchange resin) to replace ions of Br^- with ions of OH^-. The $HM(OH)_2$ aqueous solution was concentrated at 35 Torr and 30 °C until the hydroxide concentration was > 1.0 M (measured by titration with 0.01 M HCl using methyl red as indicator).

4.3. Synthesis of germanosilicate zeolites

4.3.1. IWW

Zeolite IWW-2 with Si/Ge = 2 in the reaction gel (Table 3) was synthesized following the procedure reported in Ref.[17] The reaction mixture was composed of TEOS, GeO_2, $MPP(OH)_2$ and distilled water. For the synthesis of IWW-2, 0.73 g of GeO_2 was added to 3.8 ml of 1M $MPP(OH)_2$ solution mixed with 3.4 ml of distilled water. After the dissolution of GeO_2, 3.1 ml of TEOS was added to the mixture dropwise and the gel was stirred for 30 min at room temperature for 30 min. The prepared mixture was placed in the autoclave and crystallised under rotation (60 rpm) at 175 °C for 7 days. After that, the autoclave was cooled down with water. The solid product was isolated by filtration, washed with distilled water and ethanol, and dried at 60 °C overnight. The sample was calcined at T = 550 °C with a heating rate of 1 oC/min the airflow for 4 h and used for seeding of reaction mixtures with variable Si/Ge ratios (Table 3). The seeds were added to reaction mixtures of different compositions just before loading it into the autoclave. The samples were named IWW-n, where n corresponds to the Si/Ge ratio used for the preparation of germanosilicate (according to Table 3).

Table 3: Composition of the reaction mixture for IWW samples (in mols)

Name	Si/Ge molar ratio	SiO_2	GeO_2	$MPP(OH)_2$	H_2O	IWW-2 seeds
IWW-2	2	0.66	0.33	0.25	15	-
IWW-4	4	0.72	0.20	0.25	15	
IWW-6	6	0.76	0.14	0.25	15	
IWW-8	8	0.80	0.11	0.25	15	
IWW-10	10	0.82	0.09	0.25	15	0.08
IWW-12	12	0.88	0.08	0.25	15	
IWW-14	14	0.90	0.07	0.25	15	
IWW-16	16	0.09	0.06	0.25	15	

4.2.2. ITH

ITH zeolites were prepared according to Ref.[57] The reaction mixture consisted of TEOS, GeO_2, $HM(OH)_2$, HF, and distilled water. For the synthesis of ITH-10 with Si/Ge = 10 in the reaction mixture (Table 4), 0.20 g of GeO_2 was added to 5.00 ml of 1M $HM(OH)_2$ and stirred. After the dissolution of GeO_2, 4.31 ml of TEOS was added to the mixture dropwise and the mixture was stirred for the time needed for the evaporation of an excess of water at room temperature. Finally, 0.45 ml of HF was added to the gel mixture, the gel formed was placed in the autoclave and subjected to crystallization at 135 °C for 24 days under static conditions. After this time, the autoclave was cooled down with water. The solid product was isolated by

filtration, washed with distilled water and ethanol, and dried at 60 °C overnight. The sample was calcined at 550 ° C with a heating rate of 1 oC/min air flow for 6 h. Samples with variable Si/Ge ratios (Table 4) were prepared similarly to ITH with Si/Ge = 10, while varying the amount of TEOS and GeO_2. The samples were named ITH-n, where n corresponds to the Si/Ge ratio used for the preparation of germanosilicate (according to Table 4).

Table 4: Composition of the reaction mixture for ITH samples (in mols)

Name	Si/Ge molar ratio	SiO$_2$	GeO$_2$	MH(OH)$_2$	H$_2$O	HF
ITH-10	10	0.91	0.09	0.28	7	0.56
ITH-15	15	0.94	0.06	0.28	7	0.56
ITH-20	20	0.95	0.05	0.28	7	0.56
ITH-30	30	0.97	0.03	0.28	7	0.56

4.4. Post-synthesis degermanation/metallation

All degermanation/metallation treatments were performed according to the procedure reported in Ref.[33]

4.4.1. Preparation of Al-substituted zeolites

0.1 g of a calcined germanosilicate zeolite was treated with 10 ml of 1M $Al(NO_3)_3$ solution at 95 °C for 4 days. The solid material was filtered, washed with distilled water, dried, and calcined at 450 °C for 4 hours with a heating rate of 1 oC/min The samples were named IWW-n/Al and ITH- n/Al, where n corresponds to the Si/Ge ratio used for the preparation of the parent germanosilicate (according to Tables 3 and 4).

4.4.2. Preparation of Ti-substituted zeolites

0.4 g of calcined germanosilicate zeolite was treated with 40 ml of 0.1 M HCl solution for 4 hours at room temperature. The solid sample was isolated by filtration, washed with distilled water, and dried at 60 °C overnight. The dry sample was activated at 450 °C for 1 hour and placed in the flask with a 1 M solution of $TiCl_4$ in toluene. This mixture was stirred for 7 days or 1 day at 95 °C in a nitrogen atmosphere for ITH and IWW zeolites, respectively. The solid material was filtered, washed with toluene, dried and calcined at 450 ° C for 4 hours with a heating rate of 1 oC/min. The samples were named IWW-n/Ti and ITH-n/Ti, where n corresponds to the Si/Ge ratio used for the preparation of the parent germanosilicate (according to Table 3 and Table 4).

4.4.3. Preparation of Sn-substituted zeolites

0.4 g of calcined germanosilicate zeolite was treated with 40 ml of 0.1 M HCl solution at room temperature for 4 hours. The solid was isolated by filtration, washed with distilled water, and dried at 60 °C overnight. The dry sample was activated at 450 °C for 1 hour and placed in the flask with a 1 M $SnCl_4$ solution in toluene. This mixture was stirred for 7 days or

1 day at 95 °C in a nitrogen atmosphere for ITH and IWW zeolites, respectively. The solid material was filtered, washed with toluene, dried and calcined at 450 °C for 4 hours with a heating rate of 1 oC/min The samples were named IWW-n/Sn and ITH-n/Sn, where n corresponds to the Si/Ge ratio used for the preparation of the parent germanosilicate (according to Table 3 and Table 4).

4.5. Characterization of prepared zeolites

XRD patterns were measured on a Bruker D8 Advance diffractometer equipped with a Linxeye XE-T detector and a source of CuKα (1.5406) radiation. The sample was grinded to avoid preferential orientation of the crystals and placed on the special holder prior to the measurement.

N_2 ad-/desorption isotherms were measured at -195.8°C on a Micromeritics 3Flex volumetric Surface Area Analyzer. Before measurement, the sample was outgassed on a Micromeritics Smart Vac Prep instrument at p < 13.3 Pa and activated at T = 250 °C (achieved with a heating rate of 1 oC/min) for 8 hours. To calculate the external surface area and the micropore volume, the t-plot method was used, while the total adsorption volume was detected as the capacity at relative pressure $p/p_0 = 0.95$.

Chemical composition was determined using ICP-MS analysis on Agilent 7900 inductively coupled plasma mass spectrometry (Agilent Technologies, Inc., USA). 50 mg of the sample were mixed with 1.9 ml of HNO_3 (67 – 69%, ANALPURE®), 5.5 ml of HCl (34 – 37%, ANALPURE®), 1.9 ml of HF (47 – 51%, ANALPURE®), this mixture was placed in the closed Teflon vessel. This vessel was placed in the microwave (Speedwave® XPERT, Berghof) and heated at T = 210 °C with a ramp 5 oC/min for 25 min. This mixture was cooled and the complexation of the surplus HF complex was performed using 10 ml of H_3BO_3. The mixture was placed again in the microwave at 190 °C (the heating ramp 5 oC/min) for 10 min and the sample was diluted for analysis after cooling.

Scanning electron microscopy images were taken on a JEOL JSM-IT800 microscope, using a secondary electron detector. The powder samples were placed on copper stubs with double-sided sticky carbon tape to increase conductivity and help avoid charging effects.

IR spectra were measured using a Nicolet iS50 spectrometer with the MCT/B detector. Spectra were taken in the range of 4000 – 400 cm^{-1} with a step of 4 cm^{-1} by collecting 128 scans per a spectrum. Zeolite wafers with density 10 mg/cm^2 were prepared, outgassed at p < 13.3 Pa and activated at temperature 450 °C for 4 hours. Pyridine (for IWW-n/Al and ITH-n/Al samples) and d$_3$-acetonitrile (for IWW-n/Ti, IWW-n/Sn, ITH-n/Ti, ITH-n/Sn) were used as probe molecules to assess the total concentration of acid sites in metallated zeolites. The number of BAS, which are accessible for bulky molecules in Al-substituted zeolites was probed with 2,6-ditertbutylpyridine.

The adsorption of pyridine occurred at a temperature of 150 °C at a partial pressure of 3.5 Torr for 20 min. Evaluation of the concentration of the Lewis acid sites and Brønsted acid sites was carried out by integrating the intensities of the IR bands at 1454 cm^{-1} and 1545 cm^{-1}, respectively. Molar absorption coefficients (ε) were found in the literature[66]: $\varepsilon(1454$ cm$^{-1}) = 2.22$ cm/μmol and $\varepsilon(1545$ cm$^{-1}) = 1.67$ cm/μmol.

The adsorption of 2,6-ditertbutylpyridine in Al-containing zeolites took place at a temperature of 150 °C at equilibrium probe vapour pressure for 20 min, followed by desorption for 60 min at the same temperature. Evaluation of Brønsted acid sites, which are accessible for 2,6-ditertbutylpyridine, was carried out by integration of the intensity of the IR band at 3308 cm^{-1}. The molar absorption coefficient (ε) was found in the literature[58]: ε(3308 cm^{-1}) = 5.22 cm/µmol.

The adsorption of acetonitrile in Ti- and Sn-substituted zeolites occurred at a temperature of 25 °C at a partial pressure of 5 Torr for 20 min. The evaluation of the concentration of Lewis acid sites was done by integrating the intensities of the IR bands at 2304 cm^{-1} (Ti-containing zeolites) and 2308 cm^{-1} ($Sn(OSi)_4$ sites in Sn-substituted zeolites) and 2316 cm^{-1} ($Sn(OH)(OSi)_3$ sites in Sn-substituted zeolites). Molar absorption coefficients (ε) were found in the literature: ε(2304 cm^{-1}) = 0.83 cm/µmol,[59] ε(2308 cm^{-1}) = 2.04 cm/µmol[60] and ε(2316 cm^{-1}) = 1.04 cm/µmol.[60]

UV-vis diffuse reflectance spectra were measured in a wavelength range of 200 – 600 nm using the Varian 4000 UV-vis spectrometer (Agilent). The diffuse reflectance spectra were converted into absorption spectra using the Kubelka- Munk function.

5. Results and discussion

4.1. Parent germanosilicate zeolites with different Si/Ge ratios

4.1.1. Zeolite crystallization vs. Si/Ge

For the synthesis of zeolites IWW-n, the Si/Ge molar ratio in the reaction mixture was varied from 4 to 16 in the presence of MPP(OH)$_2$ as SDA. Because pure phase IWW was previously reported to be formed only in the ranges of Si/Ge = 1.0 – 6.6,[17,18] seeding with IWW-2 was applied to expand this range. The XRD patterns of the materials isolated from the reaction mixtures with different chemical compositions are compared in Figure 14 with that of the reference IWW framework from the database of Structure Commission of the International Zeolite Association (IZA-SC).[2] Zeolite IWW can be identified according to some characteristic peaks, such as 4.20, 6.98, 8.00, 8.34 9.30, 10.00, 10.64 2θ, well observed for all synthesised samples. For samples prepared in reaction mixtures with Si/Ge = 12 – 16, in addition to the characteristic diffraction lines of IWW zeolite, additional reflexes were observed (marked with asterisks 8.80, 17.29, 19.21, 23.27 2θ in Figure 14). To specify the structure of the material present in addition to IWW in the final mixture, the analysis of XRD patterns was performed. By comparison with IZA database, it was found that the zeolite that was formed as an admixture in the IWW-12 – IWW-16 samples is a zeolite with MEL topology.
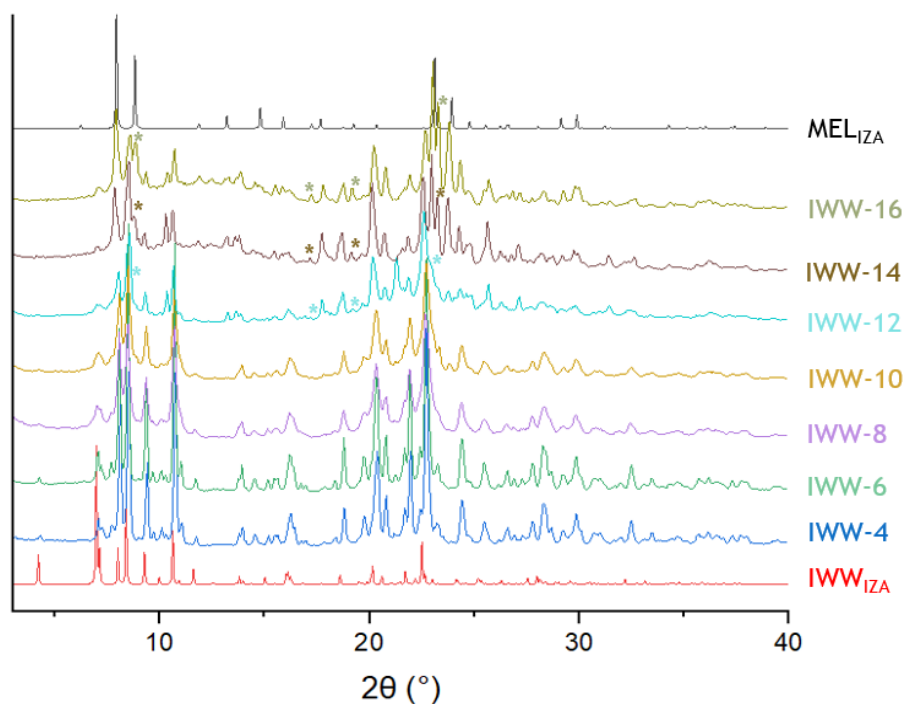

Figure 14: XRD diffractograms of zeolites prepared with different Si/Ge ratios in the presence of MPP(OH)$_2$ as SDA. The experimental XRD patterns are compared with the reference diffractograms of IWW and MEL zeolites taken from the International Zeolite Association (IZA) database.[2] The peaks typical for MEL admixture are shown with asterisks in IWW- 12, - 14, -16 samples.

Thus, using seed-assisted crystallization enabled the synthesis of pure IWW zeolites in the Si/Ge range of 4 to 10, which is larger compared to previously reported one. Further increase in the Si/Ge ratio (Si/Ge > 10) in reaction mixture leads to formation of an additional phase of MEL zeolite.

ITH-n zeolites with the same type of structure but variable chemical composition were synthesised in reaction mixtures with Si/Ge ratios ranging from 10 to 30. After syntheses, the measured XRD patterns (shown in Figure 15) were compared with the reference XRD pattern of ITH zeolite from IZA-SC. The presence of all characteristic diffraction lines of ITH and the lack of any other peaks for the samples ITH-10 – ITH-30 samples confirm the phase purity of the synthesized samples.
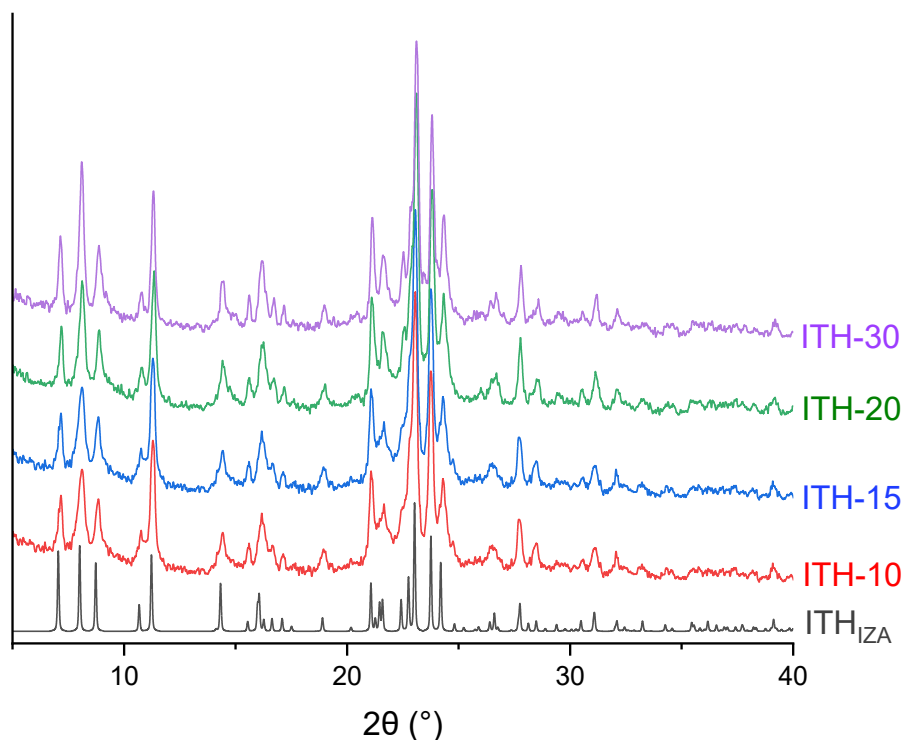

Figure 15: XRD diffractograms of zeolites prepared with different Si/Ge ratios in the presence of HM(OH)₂ as SDA. The experimental XRD patterns are compared with the diffractograms of ITH zeolites taken from the database of the International Zeolite Association (IZA).

XRD analysis enabled characterization of the phase purity of germanosilicate zeolites prepared using reaction mixtures with different Si/Ge ratios. Based on the obtained results, the phase pure IWW-4 – IWW-10 and ITH-10 – ITH-30 samples were selected for further analysis of the influence of the Si/Ge ratio on the textural characteristics of germanosilicate zeolites and physicochemical properties of Al-, Ti-, Sn-substituted materials prepared by the degermanation/metallation approach.

4.1.2. Physicochemical properties vs. chemical composition in germanosilicate zeolites

Table 5 shows the chemical composition of IWW and ITH zeolites prepared from reaction mixtures with different Si/Ge ratios as described in the previous section. The concentration of Ge in both IWW and ITH zeolites progressively decreased (so the Si/Ge ratio increased) with the decrease in the concentration of Ge in reaction mixture. Generally, solid samples showed lower Si/Ge in the comparison to Si/Ge in reaction mixture. For example, IWW-6 was characterized by Si/Ge = 5 measured by chemical analysis, while IWW-10 showed Si/Ge = 8. In turn, ITH-10 had Si/Ge = 6 in the sample, while ITH-30 was characterized by Si/Ge = 21. This result indicates a higher fraction of Ge atoms incorporated into zeolite frameworks in comparison to Si.

The influence of the Si/Ge ratio in the reaction mixture on the size and shape of the IWW and ITH zeolite crystals was studied by SEM. Figures 16 and 17 show two sets of SEM images for IWW and ITH crystals, respectively, while the images in each set have the same magnification. The IWW-2 zeolite crystallised in the form of rectangular prisms with dimensions a = 2.11 μm; b = 1.10 μm; c = 0.20 μm. An increase in the Si/Ge ratio results in significant shortening of the two crystal dimensions. For example, crystals of IWW-8 (0.75 x 0.07 x 0.03 μm) and IWW-10 (0.69 x 0.04 x 0.04 μm) with the highest Si/Ge ratios grow in the shape of thin needles aggregated in fans. Some larger rectangular crystals seen in the SEM image of IWW-10 zeolite can be assigned to the seeds used in the synthesis mixture. The influence of the Si/Ge ratio on the IWW zeolite crystal size may be caused by the effect of the Ge on different steps of the crystallisation process, such as nucleation and crystal growth. For a clarification of the mechanism of the Ge effect, detailed kinetic studies of the crystallization process are required.

Table 5: Chemical composition and textural properties of zeolite samples synthesized from reaction mixtures with different Si/Ge ratios

Sample	Si/Ge (ICP-MS)	V_{micro} (cm^3/g)	V_{tot} (cm^3/g)	S_{ext} (m^2/g)	Crystal size (μm)
IWW-4	4	0.19	0.23	58	2.11 x 1.10 x 0.20
IWW-6	5	0.18	0.23	73	2.77 x 1.37 x 0.24
IWW-8	6	0.17	0.33	105	0.75 x 0.07 x 0.03
IWW-10	8	0.16	0.36	120	0.69 x 0.04 x 0.04
ITH-10	6	0.12	0.15	34	5.18 x 0.34 x 0.13
ITH-15	10	0.12	0.19	57	5.53 x 0.46 x 0.15
ITH-20	12	0.14	0.20	52	5.65 x 0.48 x 0.15
ITH-30	21	0.14	0.18	57	7.75 x 1.19 x 0.16

In contrast to IWW zeolites, the effect of the Si/Ge ratio on the size and shape was not so pronounced in the studied range of Si/Ge ratios (Table 5). Specifically, all ITH zeolites crystallized from reaction mixtures with Si/Ge = 10 – 30 swarm into thin, narrow rectangles agglomerated into fan-like species. The difference in the observed effect of Ge concentration in the reaction mixture on crystal size and shape may be caused by the difference in the studied Si/Ge ratio range for these systems (e.g., Si/Ge = 2 – 10 for IWW and Si/Ge = 10 – 30 for ITH) as well as by different distributions of Si and Ge between different crystallographic positions in two zeolites.

The nitrogen physisorption results for ITH and IWW germanosilicates agree with the data of SEM analysis. The respective ad-/desorption isotherms are shown in Figure 18, while the textural characteristics of the samples with a varied Si/Ge ratio are presented in Table 5. The zeolites IWW-4, IWW-6 and ITH-10 show Type I(a) adsorption isotherms typical of microporous materials (as described in Section 3.3.3. Physisorption). In turn, zeolites IWW-8,
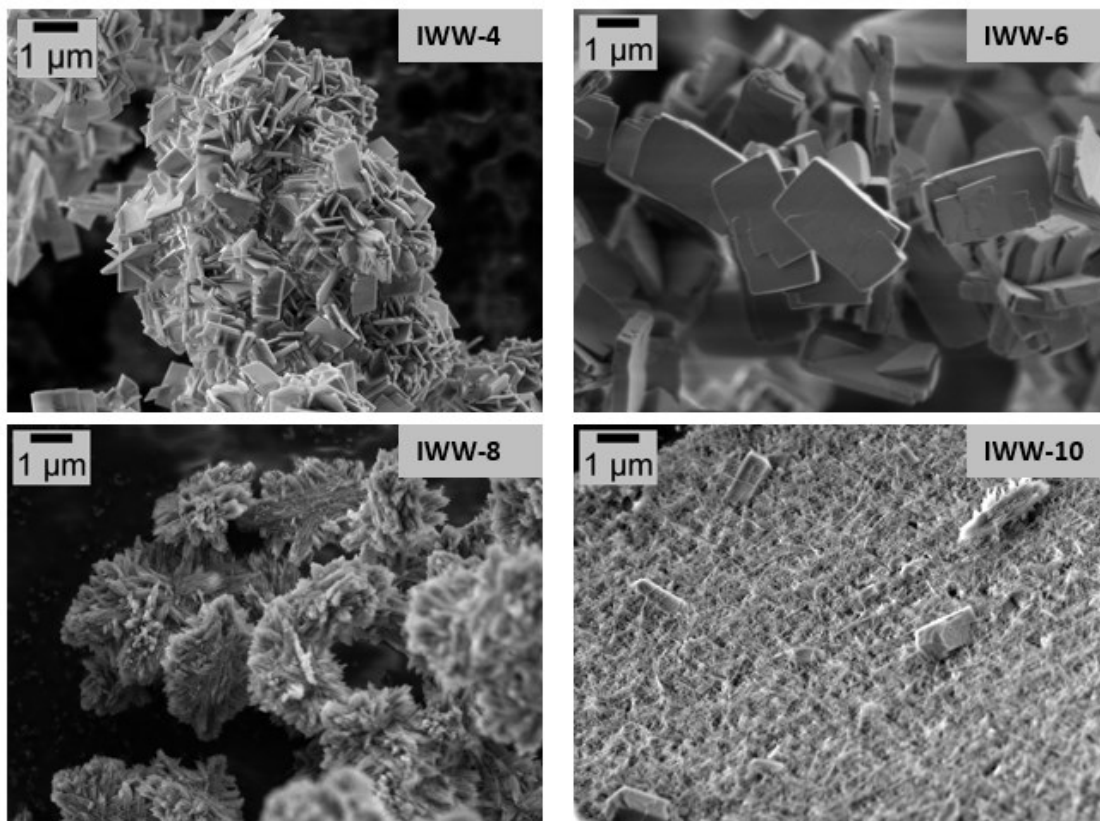
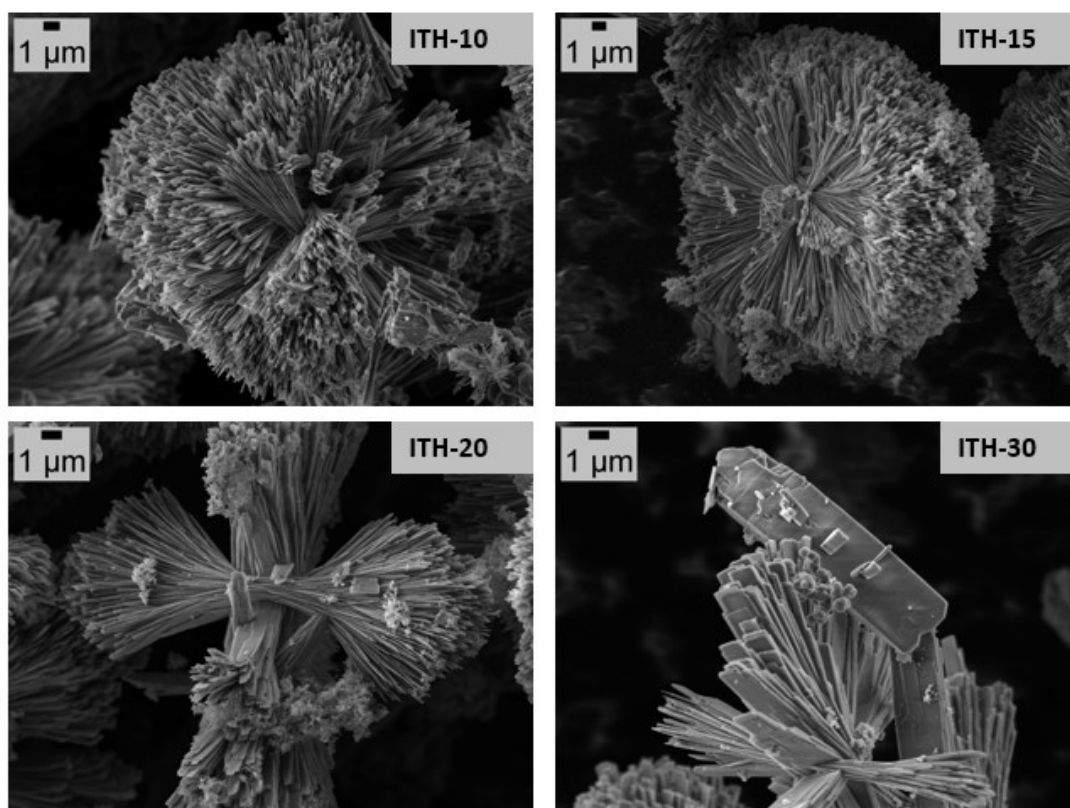*Figure 16: SEM images of IWW-n zeolites with different Si/Ge ratios*

Figure 17: SEM images of ITH-n zeolites with different Si/Ge ratios.

IWW-10, ITH-15, ITH-20, and ITH-30 have isotherms of combined Type-I(a) and Type-IV(a) with a hysteresis loop. Nitrogen uptake at $p/p_0 < 0.05$ corresponds to micropore filling, while that at $p/p_0 > 0.5$ arises from adsorption in intercrystalline voids present in samples characterised by small crystal size. Adsorption in the intercrystalline voids takes place at pressures higher than those of desorption, leading to the appearance of a hysteresis loop. In particular, intercrystalline porosity was not documented for zeolites IWW-4, IWW-6, and ITH-10 with relatively large crystals (Table 5).
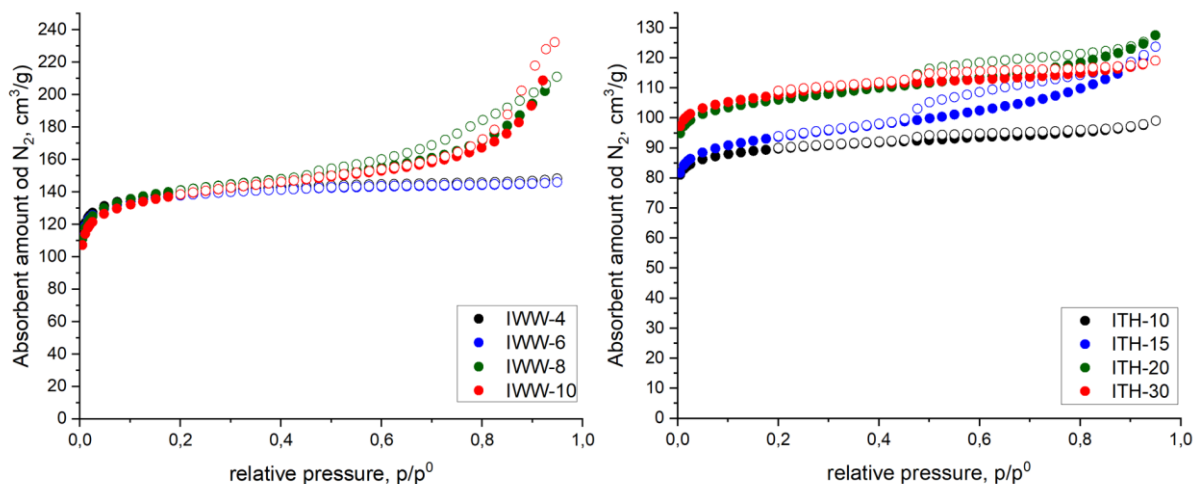

Figure 18: Nitrogen adsorption (●) and desorption (○) isotherms for IWW-n (left) and ITH-n (right) zeolites with different Si/Ge ratios.

Three main textural characteristics were evaluated from the nitrogen adsorption isotherms. Namely, we consider the external surface area (S_{ext}), the micropore volume (V_{micro}), and the total pore volume (V_{tot}). All these values are given in Table 5. As can be seen from the measured data, the external surface area progressively increases from 58 to 120 m^2/g with a decrease in the crystal size of the IWW samples. Consistent with the marginal effect of the Si/Ge ratio on the crystal size of the ITH zeolite, after increase of S_{ext} from 34 to 57 m^2/g with increasing Si/Ge ratio in ITH-10 and ITH-15, S_{ext} value was maintained for ITH-15 – ITH-30 samples at 52 – 57 m^2/g.

The micropore volumes of the IWW samples decreased slightly with an increase in the Si/Ge ratios (0.19 and 0.16 cm^3/g for IWW-4 and IWW-10, respectively), while the total volume increased (0.23 and 0.36 cm^3/g for IWW-4 and IWW-10, respectively). The increase in the total pore volume is probably caused by the development of intercrystalline porosity as the size of the zeolite crystals decreases.

The results clearly indicate the influence of Si/Ge in the reaction mixture on the size and shape of the IWW zeolite crystals, thus affecting their textural properties. This effect can be used for regulation of intracrystalline paths for reacting molecules within IWW zeolite catalysts after incorporation of active metal sites and, as a result, to manipulate their productivity and optionally shape-selectivity.

4.2. Degermanation/metallation of IWW and ITH zeolites with different Si/Ge ratios

To investigate the influence of the Si/Ge molar ratio of the parent germanosilicates on the physicochemical characteristics of Al-, Ti-, and Sn-substituted zeolites prepared by the degermanation/metallation approach, post-synthesis modification of the IWW-n (n = 4 – 10) and ITH-n (n = 10 – 30) samples was carried out according to Ref.[33] Treatment of germanosilicates in acidic medium (e.g., with 1M $Al(NO_3)_3$ at pH = 2 for the synthesis of Al-substituted zeolites or with 0.01 M HCl at pH = 2 for the synthesis of Ti- and Sn-substituted zeolites) resulted in 1) removal of a part of Ge and 2) increased amount of incorporated metal in degermanated/metallated samples (Table 6). Observation 1) is in line with the hydrolysis of Ge-O bonds in an acidic medium. In particular, ca. 70 % of Ge was removed from IWW-n independently of the Si/Ge ratio in the parent zeolite (shown for n = 4 and 6 in Table 6), while ITH-n showed a lower degermanation degree, which decreased with increasing Si/Ge ratio in the parent zeolite. For example, 34 % of Ge was removed from the ITH-10 sample, while the degree of degermanation of ITH-30 was 16 %. The lower degermanation degree of ITH *vs.* IWW zeolite may be related to the smaller size of the pores in the former zeolite (10-10-9-ring and 12-10-8 ring pores in ITH and IWW, respectively), which can hinder the access of hydrolysing agents to Ge sites.

Table 6: Chemical composition of zeolite samples synthesized with different Si/Ge ratio and subjected to degermanation/metallation treatment

Parent zeolite	Incorporated Metal	Metal (mol.%)	Ge (mol. %)	Si (mol. %)	ΔGe, %[a]	V_{micro} (cm^3/g)	V_{tot} (cm^3/g)	S_{ext} (m^2/g)
IWW-4	-	-	19.2	80.8	0	0.19	0.23	58
	Al	5.7	5.7	88.6	73	0.20	0.29	143
	Sn	3.1	5.5	91.4	75	0.10	0.20	118
	Ti	15.2	5.3	79.5	72	0.16	0.27	139
IWW-10	-	-	11.4	88.6	0	0.16	0.36	120
	Al	4.4	3.5	92.1	70	0.17	0.29	145
	Sn	3.6	3.6	92.8	70	0.11	0.44	205
	Ti	15.7	3.7	80.6	64	0.09	0.22	136
ITH-10	-	-	15.3	84.7	0	0.12	0.15	34
	Al	2.1	10.4	87.5	34	0.12	0.19	100
	Sn	n.s.[b]	n.s.[b]	n.s.[b]	n.s.[b]	0.08	0.09	55
	Ti	n.s.[b]	n.s.[b]	n.s.[b]	n.s.[b]	0.05	0.09	56
ITH-30	-	-	4.6	95.4	0	0.14	0.18	57
	Al	0	3.9	96.1	16	0.13	0.21	89
	Sn	n.s.[b]	n.s.[b]	n.s.[b]	n.s.[b]	0.08	0.14	53
	Ti	n.s.[b]	n.s.[b]	n.s.[b]	n.s.[b]	0.09	0.05	53

a – degermanation degree, calculated as the fraction of Ge removed from parent germanosilicate, %;

b – not studied.

The structure and phase composition of degermanated/matallated zeolites were studied using XRD. Figure 19 and 20 compare the XRD patterns of parent IWW and ITH zeolites with the lowest and the highest studied Si/Ge ratios with those of post-synthetically degermanated/metallated samples. The features further described for the respective series of

samples were observed for the whole set of degermanated/metallated IWW and ITH zeolites, respectively. In general, degermanated/metallated samples demonstrated lower crystallinity (wider diffraction lines) compared to the parent germanosilicate zeolites. This result is probably caused by the partial disorder during several steps of chemical transformations upon post-synthesis treatments, namely removal of Ge atoms and incorporation of metal atoms. Independently of the n-value, post-synthesis IWW-n/metal and ITH-n/metal samples showed the same position of characteristic diffraction lines as the parent zeolites, but with modified relative intensities. For example, the typical feature of all degermanated/metallated IWW samples is an increase in the relative intensity of the diffraction line d_{110} at 7.1 2θ (marked in Figure 19 with a bluish line), which may be caused by changing the chemical composition at specific positions of the framework.
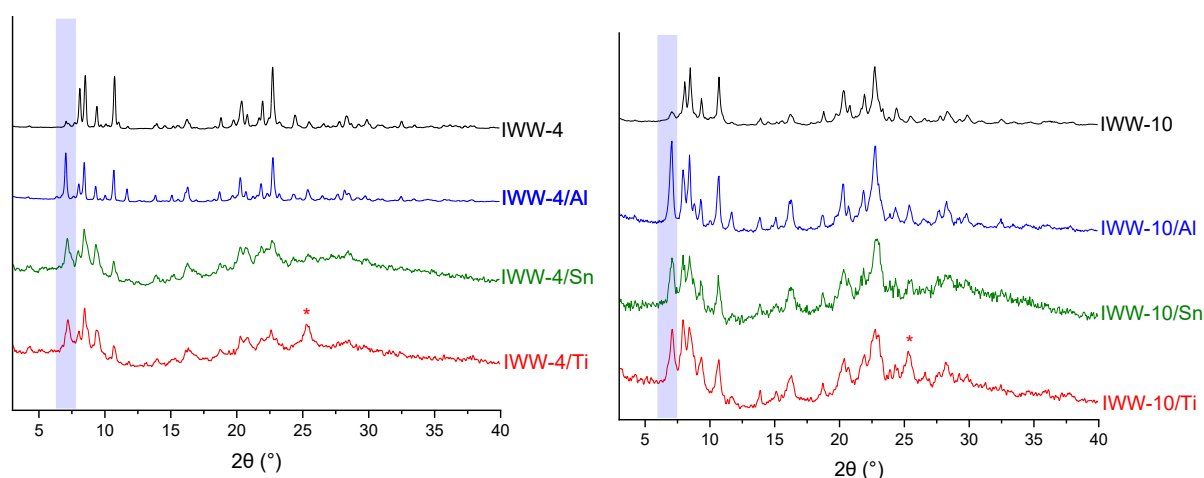

Figure 19 XRD patterns for post-synthesis IWW-4 (left) and IWW-10 (right) zeolites.
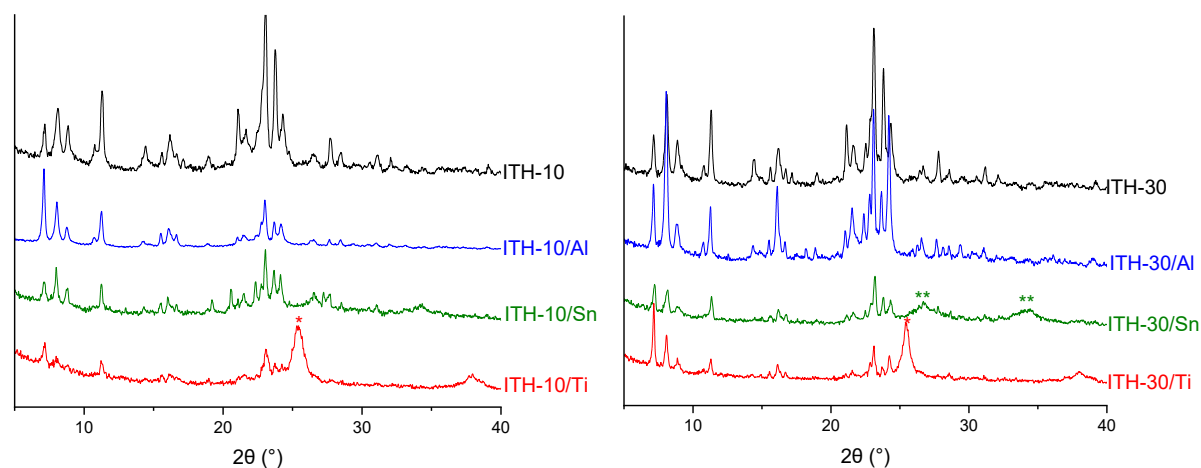
Figure 20: XRD patterns for post-synthesis ITH-10 (left) and ITH-30 (right).

Both Al-substituted IWW-n/Al and ITH-n/Al series of materials and Sn-substituted IWW-n/Sn zeolites show no signs of admixed phases. In contrast, the XRD patterns of all IWW-n/Ti and ITH-n/Ti demonstrated the appearance of an additional diffraction line at 25.2 2θ (marked in Figure 19 and Figure 20 with *), indicating the formation of the TiO_2 anatase phase.[61] Unlike the IWW-n/Sn series and ITH-10/Sn sample, Sn-substituted ITH-n/Sn zeolites with

n = 15, 20, 30 show the presence of the SnO_2 cassiterite phase, indicated by the diffraction lines at 26.7 and 33.4 2θ (marked in Figure 20 with **).[62]

Table 6 compares the textural properties of the parent germanosilicate zeolites with the lowest and highest achieved Si/Ge ratios (i.e., IWW-4, IWW-10, and ITH-10, ITH-30) on one side, and the characteristics of post-synthetically degermanated/metallated samples on another side. Al-substituted zeolites showed similar or higher V_{micro} and V_{tot} values compared to parent germanosilicates, which can be explained by the decrease in density of the material after the substitution of Ge atoms (M_w^{Ge} = 72 g/mol) with Al atoms (M_w^{Al} = 27 g/mol) accompanied with preservation of the framework and absence of pore blocking. At the same time, Sn- and Ti-containing samples showed lower values compared to the starting germanosilicate samples. This result may be related to the formation of extraframework TiO_2 and SnO_2 species in post-synthesised zeolites (as evidenced by XRD analysis), leading to partial occupation of the zeolite pore systems by these admixtures.
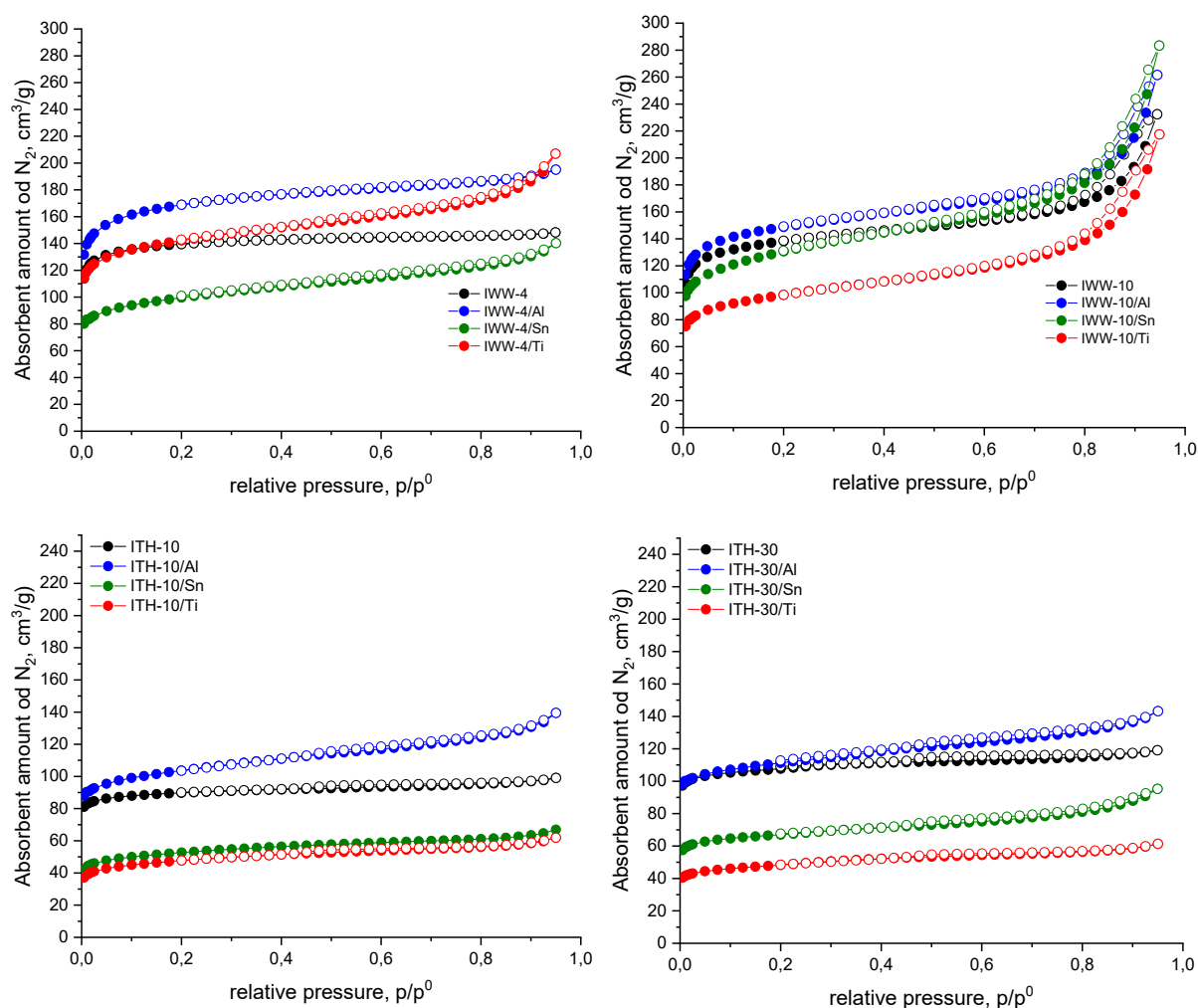

Figure 21: Nitrogen adsorption (●) and desorption (○) isotherms for degermanated/metallated IWW-4 (top, left), IWW-10 (top, right), ITH-10 (bottom, left), ITH-30 (bottom, right) zeolites.

Metal-containing zeolites derived from IWW-4 and ITH-10 with the lowest Si/Ge in the respective series were characterized by 1.6 – 2.9 times higher S_{ext} values compared to the parent

germanosilicates. For example, for the IWW-4 series, S_{ext} increased in the following sequence: IWW-4 (58 m^2/g) < IWW-4/Sn (118 m^2/g) < IWW-4/Ti (139 m^2/g) = IWW-4/Al (143 m^2/g). Similarly, for the ITH-10 series, S_{ext} increased as follows:

ITH-10 (34 m^2/g) < ITH-10/Sn (55 m^2/g) = ITH-10/Ti (56 m^2/g) < ITH-10/Al (100 m^2/g). This result can be explained by the development of mesopores upon degermanation and non- equivalent replacement of Ge for Al, as reported in Ref.63,64 In line with this observation, the respective degermanated/metallated zeolites (e.g., IWW-4/Sn, IWW-4/Ti, IWW-4/Al and ITH-10/Al) showed a steeper slope of adsorption isotherms at p/p0 > 0.05, corresponding to the filling of mesopores (Figure 21). An increase in Sext was also observed, but less pronounced for metal-containing zeolites derived from materials with the highest Si/Ge, IWW-10, and ITH-30 (Table 6).

The coordination state of metal sites in the Ti- and Sn-substituted samples was further verified using UV-vis spectroscopy (Figure 22 and 23). The UV-vis spectra of Ti-substituted IWW-n/Ti and ITH-n/Ti zeolites showed broad bands at ~230 nm (assigned to tetrahedrally coordinated framework Ti species), ~265 nm (assigned to extra-framework Ti) and ~320 nm (assigned to bulky TiO_2).[54] The amount of Ti atoms incorporated into the framework positions (based on the relative intensity of the band at ~230 nm) of IWW-8 zeolite was higher compared to the ITH-10 sample with a similar Si/Ge ratio at 6 (Table 5). Within the IWW-n/Ti series, the concentration of Ti atoms (based on the intensity of the band at ~230 nm) increases in the following sequence: IWW-10/Ti < IWW-6/Ti < IWW-4/Ti < IWW-8/Ti.

Figure 22: UV-vis spectra of Ti-containing zeolites prepared via the degermanation/metallation approach of the IWW (left) and ITH (right) samples with different Si/Ge ratios

Based on the results of UV-vis spectroscopy (Figure 23, Sn-substituted IWW-n/Sn and ITH-n/Sn zeolites contained different concentrations of tetracoordinated framework Sn species (absorption band at 210 nm), extraframework Sn (absorption band at 240 nm) and bulk SnO_2 (absorption band at 300 nm) (Figure 23).[56] Similarly to Ti-substituted samples prepared using ITH-10 and IWW-8 zeolites with the same Si/Ge ratio, ITH-10/Sn was characterized by a significantly higher fraction of bulk SnO_2 phase compared to IWW-8/Sn. The deposition of the larger amount of extra-framework oxide species upon metalation of ITH zeolite may be related to 1) the lower degermanation degree of ITH *vs.* IWW (Table 6), which causes limited

formation of vacant sites for the incorporation of metal atoms into the ITH framework; and 2) more restricted transport of the incorporating Ti and Sn species to the framework positions of ITH with smaller micropores compared to IWW (Figure 4). The concentration of Sn atoms (based on the intensity of the band at ~210 nm) increases in the following sequence:

IWW-10/Sn < IWW-4/Sn < IWW-6/Sn < IWW- 8/Sn and

ITH-10/Sn < ITH-20/Sn < ITH- 30/Sn = ITH-15/Sn.

Notably, degermanation/metallation of IWW-10 with the lowest Ge concentration resulted in Ti- and Sn-substituted zeolites with the lowest concentration of framework tetravalent elements. This may be caused by a small number of vacant sites, that are formed after leaching of Ge from parent IWW-10. In turn, degermanation/metallation of IWW-4 with the highest concentration of Ge resulted in materials with moderate concentration of framework tetravalent elements. This is likely caused by a longer transport path, which tetravalent elements must overcome within large crystals of IWW-4 to reach the vacant sites. Notably, the post-synthesis modification of IWW-8 with moderate Ge concentration and crystal size allowed the incorporation of the highest amount of Ti and Sn into the zeolite framework.
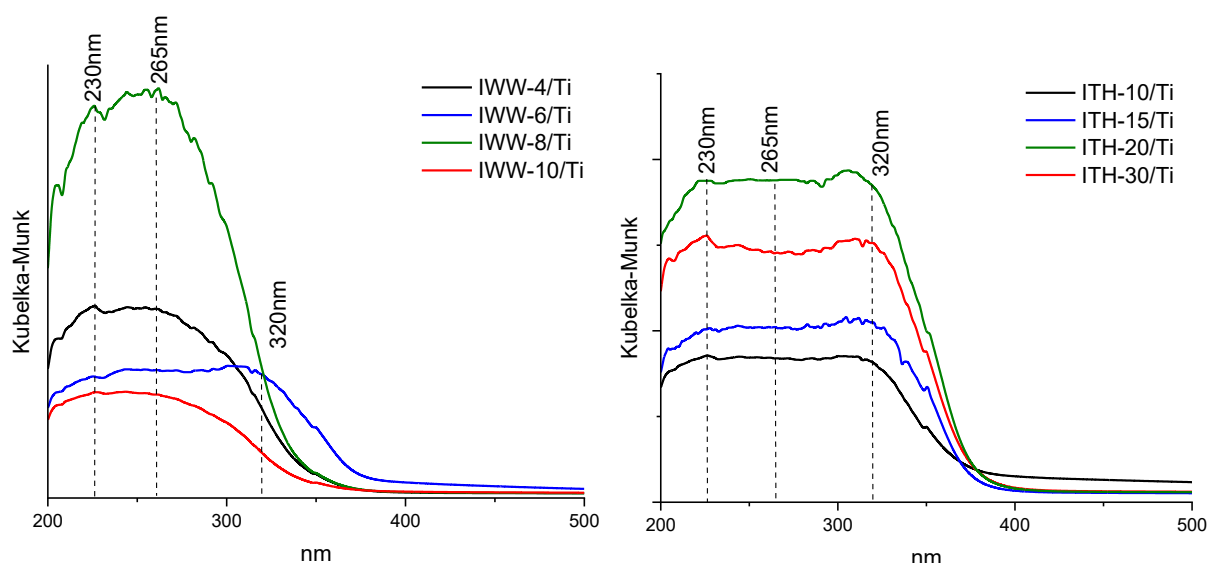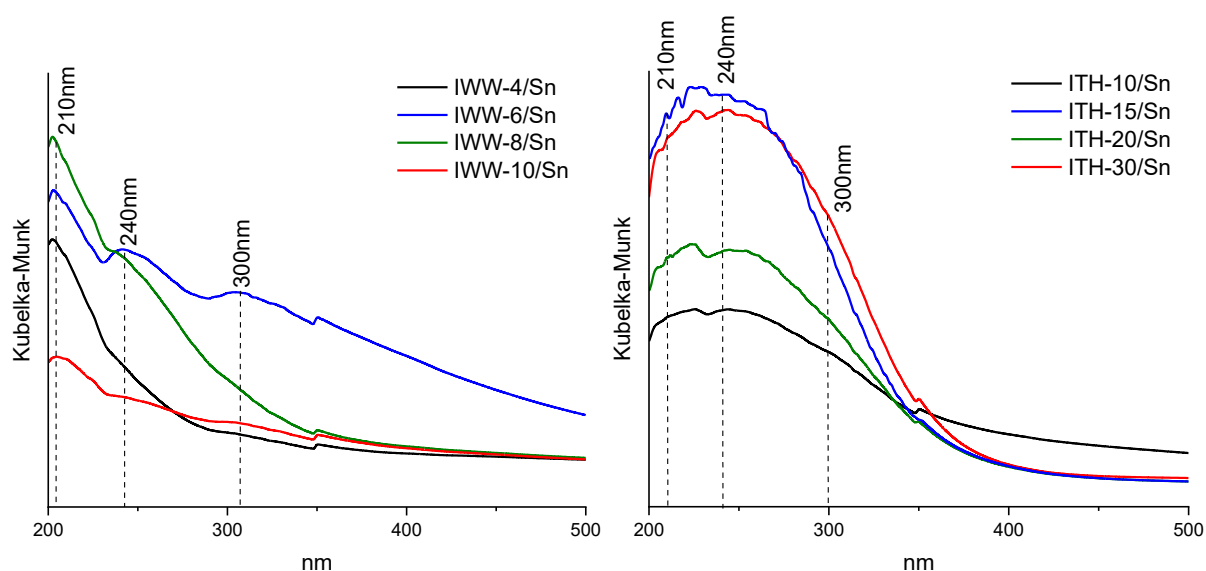

Figure 23: UV-vis spectra of Sn-containing zeolites prepared via degermanation/metallation approach of IWW (left) and ITH (right) samples with different Si/Ge ratios

Last but not least, the nature and concentration of acid sites in post-synthetically degermanated/metallated IWW-n and ITH-n zeolites were studied using IR spectroscopy of adsorbed probe molecules. Pyridine (kinetic diameter 0.54 nm) and 2,6-ditertbutylpyridine (kinetic diameter 0.79 nm) were used to study the acidic properties of Al-substituted zeolites (Figure 24), while the adsorption of d_3-acetonitrile (kinetic diameter 0.40 nm) was used to assess the acidic characteristics of Ti and Sn-substituted materials (Figure 25).[65]

The adsorption of pyridine in Al-free germanosilicate led to the low-intensive absorption band at ca. 1450 cm^{-1} corresponding to weak Ge LAS [66] (Figure 24), while degermanated/metallated IWW-n/Al and ITH-n/Al samples showed the characteristic absorption bands of the pyridine that interacts with BAS (1545 and 1638 cm^{-1}) and LAS (1455 and 1622 cm^{-1}). This result confirms a lack of acid sites interacting with pyridine in the initial germanosilicate zeolites and a functionalisation of the studied germanosilicates with Al acid sites *via* the degermanation/metallation approach.
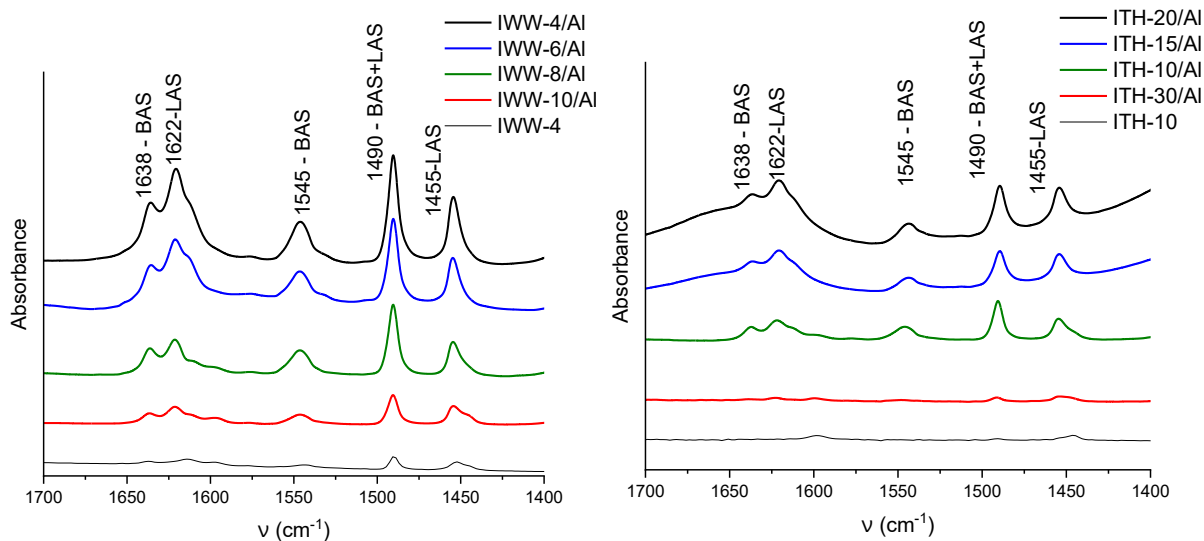
40

Figure 24: FTIR spectra of IWW (left) and ITH (right) zeolites in pyridine ring vibration region after ad-/desorption of pyridine at T = 150 °C.

Notably, the concentration of thus generated Al acid sites increased with the decrease in the Si/Ge ratio in both IWW and ITH parent germanosilicates (Table 7). Therefore, the highest concentration of Al acid sites was achieved for IWW-4/Al (0.59 mmol/g) and ITH-10/Al (0.36 mmol/g) samples prepared from IWW-4 and ITH-10 samples with the lowest Si/Ge ratios in each series. This result contrasted with the trend observed for Ti- and Sn-substituted series, where the maximum concentration of framework element was achieved for the samples prepared using IWW-8 germanosilicate with moderate Si/Ge ratio and small crystal size. This indicates a more complex character of the degermanation/metallation process for Ti and Sn, probably, affected not only by chemical factors (pH of the medium, metal concentration, number of defects formed for samples with variation in Si/Ge, etc.) but also by diffusion differences for samples with different sizes and shapes of crystals. Nevertheless, the decrease in the crystal size of the IWW zeolites increased the fraction of BAS detectable with bulky 2,6-ditertbutylpyridine:

IWW-4/Al (20 %) ≈ IWW-6/Al (17 %) < IWW-8/Al (39 %) ≈ IWW-10/Al (44 %). In contrast to IWW-n/Al, a minority of BAS is accessible for 2,6-ditertbutylpyridine in ITH-n/Al zeolites with smaller pores and larger crystals.

In turn, adsorption of d_3-acetonitrile in parent germanosilicates (IWW-4 is shown in Figure 25 as an example) gives rise to the absorption bands corresponding to the C-D bond vibrations in d_3-acetonitrile (2250 cm^{-1}), and the C≡N bond vibration in the physisorbed probe molecule (2265 cm^{-1}), hydrogen-bonded probe molecule (2275 cm^{-1}), and d_3-acetonitrile bonded with Ge sites (low-intensive band at 2306 cm^{-1}). [30,52] In addition to the mentioned bands, the spectra of IWW-n/Ti and ITH-n/Ti showed the absorption band corresponding to Ti-associated LAS (2304 cm^{-1})[50], while in the spectra of IWW-n/Sn and ITH-n/Sn the band appeared at 2310 cm^{-1} corresponds to Lewis acid sites associated with Sn (Figure 25).[51]

Table 7: The acid site concentrations for the prepared zeolites as determined using FTIR spectroscopy of adsorbed pyridine, d_3-acetonitrile and 2,6-ditertbutylpyridine

Incorporated Metal	Sample	[BAS], (mmol/g)	[LAS], (mmol/g)	Σ, (mmol/g)	[BAS] ext (mmol/g)
Al	IWW-4/Al	0.34 [a]	0.25 [b]	0.59	0.07 (20 %) [c]
	IWW-6/Al	0.25 [a]	0.19 [b]	0.44	0.04 (17 %) [c]
	IWW-8/Al	0.18 [a]	0.12 [b]	0.30	0.07 (39 %) [c]
	IWW-10/Al	0.09 [a]	0.07 [b]	0.16	0.04 (44 %) [c]
	ITH-10/Al	0.25 [a]	0.11 [b]	0.36	< 0.01 [c]
	ITH-15/Al	0.15 [a]	0.07 [b]	0.22	
	ITH-20/Al	0.10 [a]	0.07 [b]	0.17	
	ITH-30/Al	0.04 [a]	0.01 [b]	0.05	
Ti	IWW-4/Ti	-	0.32	0.32	-
	IWW-6/Ti	-	0.11	0.11	-
	IWW-8/Ti	-	0.25	1.03	-
	IWW-10/Ti	-	0.59	0.59	-
	ITH-10/Ti	-	0.12	0.12	-
	ITH-15/Ti	-	0.64	0.64	-
	ITH-20/Ti	-	0.77	0.77	-
	ITH-30/Ti	-	0.62	0.62	-
Sn	IWW-4/Sn	-	n.s. [d]	n.s. [d]	-
	IWW-6/Sn	-	0.39 [e]	0.39	-
	IWW-8/Sn	-	0.35 [e]	0.35	-
	IWW-10/Sn	-	n.s. [d]	n.s. [d]	-
	ITH-10/Sn	-	0.07 [e]	-	-
	ITH-15/Sn	-	0.07 [e]	-	-
	ITH-20/Sn	-	0.08 [e]	-	-
	ITH-30/Sn	-	0.03 [e]	-	-

a – based on the FTIR spectroscopy of adsorbed pyridine (a.b. at 1545 cm^{-1})
b – based on the FTIR spectroscopy of adsorbed pyridine (a.b. at 1450 cm^{-1})
c – based on the FTIR spectroscopy of adsorbed d_3-acetonitrile (a.b. at 2303 – 2318 cm^{-1})
d – not studied
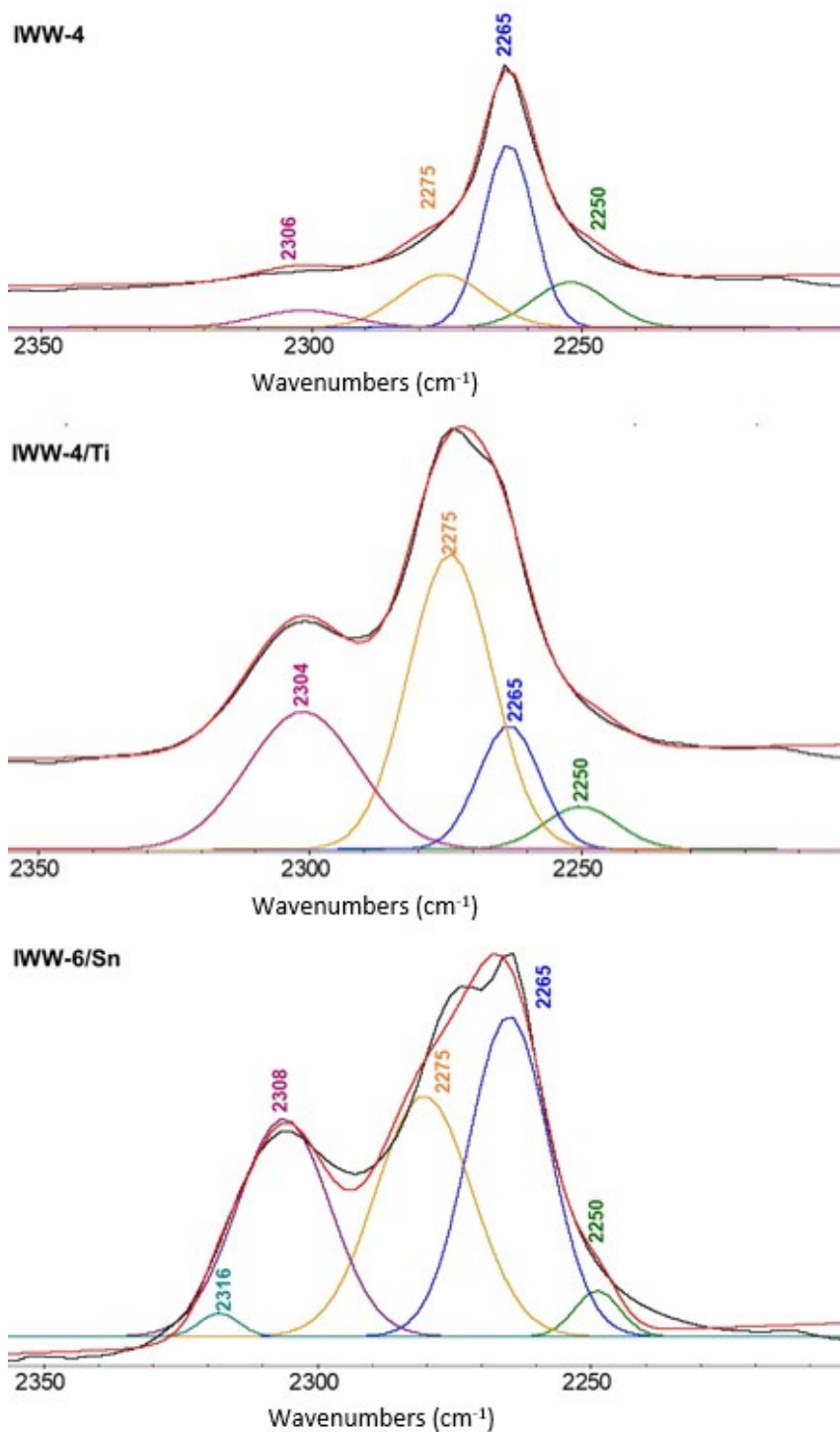e – based on the FTIR spectroscopy of adsorbed 2,6-ditertbutylpyridine (a.b. at 1540 cm^{-1})

Figure 25: FTIR spectra of IWW-4 (top), IWW-4/Ti (middle), and IWW-6/Sn (bottom) after adsorption of d₃-acetonitrile. The experimental spectra are shown in violet, while the red curve represents the results of deconvolution using Gaussian peaks.

In contrast to the clear correlation of the acid site concentration of the studied phase pure Al-substituted zeolites with the chemical composition of parent germanosilicates, no apparent trend was found for the concentration of the detectable Ti and Sn acid sites in the respective IWW-n/metal and ITH-n/metal series. Accessibility of acid sites in tetravalent element-substituted samples may be reduced by the presence of admixed TiO_2 and SnO_2 phases,

detected by XRD and UV-vis spectroscopy. For example, less LAS were detected in ITH-30/Sn (0.03 mmol/g) *vs.* ITH-10/Sn (0.07 mmol/g) with d_3-acetonitrile, despite the UV-vis spectrum of ITH-30/Sn showed a more intensive absorption band of tetracoordinated Sn generating Lewis acidity (Figure 25). This result may be rationalized considering the higher amount of SnO_2 phase in ITH-30/Sn seen in the XRD pattern of ITH-30/Sn, while ITH-10/Sn did not show diffraction lines of SnO_2 (Figure 20). Similarly, the UV-vis spectrum of IWW-6/Ti ([LAS] = 0.11 mmol/g) shows a similar intensity of the absorption band of tetracoordinated Ti as that of IWW-10/Ti ([LAS] = 0.59 mmol/g), but a more pronounced shoulder corresponding to extra-framework Ti species (Figure 22).

6. Conclusions

Recently, post-synthesis degermanation/metallation approach opened the way to zeolite materials with new structures and variable functionalities promising for catalytic applications.[6] However, the influence of the chemical composition of parent germanosilicate on the physicochemical characteristics of thus prepared Al-, Ti-, Sn-substituted zeolites has not been studied yet.

In this work, a series of Al-, Ti- and Sn-substituted zeolites were prepared using degermanation/metallation of IWW and ITH zeolites with variable Si/Ge ratios, while their physicochemical properties were studied using a set of characterization techniques, such as XRD, nitrogen physisorption, ICP-MS, UV-vis spectroscopy, and FTIR spectroscopy of adsorbed probe molecules.

The parent germanosilicate zeolites with different chemical compositions were synthesized by hydrothermal crystallization by varying Si/Ge molar ratios in the reaction mixture in the ranges of 10 – 30 and 4 – 16 for the ITH and IWW zeolites, respectively. The use of seed-assisted hydrothermal crystallization allowed us to decrease the concentration of Ge in the reaction mixture appropriate for the formation of phase pure IWW germanosilicate to Si/Ge = 10 compared to the previously reported limiting Si/Ge ratio at 6.6. The chemical composition of the parent germanosilicate zeolites ITH (Si/Ge = 6 – 21 in the samples) and IWW (Si/Ge = 4 – 8 in the samples) changed according to the composition of the reaction mixture used for hydrothermal crystallization. Although the effect of the studied Si/Ge ratios on the morphology of ITH crystals was marginal, a clear decrease in the dimensions of the IWW crystals was detected with the increase in the the Si/Ge ratio in reaction mixture. As a result, IWW zeolites formed with Si/Ge > 8 showed non-typical needle-shaped crystals.

Acidic hydrolysis of the parent germanosilicates in aluminium nitrate solution at pH = 2, resulted in Al-substituted ITH and IWW zeolites characterized by

- phase purity, preserved zeolite structure (based on XRD analysis);

- the maintained micropore volume, but increased external surface area (based on nitrogen physisorption), caused by formation of larger pore upon non-equivalent exchange of Ge for Al (based on ICP-MS);

- the presence of Brønsted and Lewis acid sites, the concentration of which increased with a decrease in the Si/Ge ratio of the parent germanosilicate (based on FTIR of adsorbed pyridine).

Acidic hydrolysis of the parent germanosilicates with hydrochloric acid at pH = 2, followed by treatment with metal source in an inert atmosphere resulted in Ti- and Sn-substituted ITH and IWW zeolites characterized by

- the preserved zeolite structure but the presence of admixed TiO_2 rutile or SnO_2 cassiterite phases (based on XRD analysis), which resulted in a decrease in the micropore volume (based on nitrogen physisorption);

- different concentrations of tetracoordinated framework metal species, extraframework metal entities, and bulk metal oxide (based on UV-vis spectroscopy). The maximal concentration of framework metal atoms achieved when using parent germanosilicate with a moderate Si/Ge

ratio and small crystal size suggests a more complex character of the degermanation/metallation process for Ti and Sn compared to Al.

The observed correlation between the concentration of Al-associated acid centers generated upon degermanation/metallation and the concentration of Ge atoms in parent germanosilicate was rationalized considering the higher number of vacant sites formed for the incorporation of Al atoms upon hydrolysis of parent zeolite with lower Si/Ge ratio. Based on the results obtained for Ti- and Sn-substituted zeolites prepared by the degermanation/metallation approach, it was proposed that incorporation of Ti and Sn in the framework positions of ITH and IWW zeolites is, probably, affected not only by chemical factors (pH of the medium, metal concentration, number of defects formed for samples with variation in Si/Ge, etc.), but also by diffusion differences existing for samples with different sizes and shapes of crystals.

A higher concentration of Al-, Ti- and Sn-associated acid sites formed upon degermanation/metallation of IWW *vs.* ITH germanosilicates with the same chemical composition (Si/Ge = 6) is in line with better transport of i) hydrolyzing agent to Ge sites and ii) hydrolyzed Ge species out of the zeolite framework through 12-10-8-ring channels of IWW compared to 10-10-9-ring pores of ITH.

The results of this B.Sc. thesis evidence that a variation in the Si/Ge ratio may result in modification of the crystal size and shape of germanosilicate zeolites and affect the state of metal atoms incorporated into zeolite by a degermanation/metallation approach.

7. List of references

1. Čejka J., Žilková N.: Chem. Listy *94*, 278 (2000).
2. http://www.iza-structure.org/databases/, download (12. 11. 2022)
3. Opanasenko M., Shamzhy M., Wang Y., Yan W., Nachtigall P., Čejka J.: Angew. Chem., Int. Ed. *59*, 19380 (2020).
4. Jorda J. L., Cantin A., Corma A., Diaz-Cabanas M. J., Leiva S., Moliner M., Rey F., Sabater M. J., Valencia S.: Z. Kristallogr.: Tenth European Powder Diffraction Conference *26*, 393 (2007).
5. Heard C. J., Grajciar L., Uhlík F., Shamzhy M., Opanasenko M., Čejka J., Nachtigall P.: Adv. Mater. (Weinheim, Ger.) *32*, 2003264 (2020).
6. Shamzhy M., Opanasenko M., Concepción P., Martínez A.: Chem. Soc. Rev. *48*, 1095 (2019).
7. Ikenna E.: Int. Res. J. Environ. Sci. *6*, 45 (2017).
8. Pophale R., Cheeseman P. A., Deem M. W.: Phys. Chem. Chem. Phys. *13*, 12407 (2011).
9. Flanigen E. M., in book: *Studies in Surface Science and Catalysis* (van Bekkum H., Flanigen E. M., Jacobs P. A., Jansen J. C., ed.), vol. *137*, p. 11. Elsevier, 2001.
10. https://chembam.com/online-resources/gcse-resources/cages/, download (8. 12. 2022)
11. Vacík J., in book: *Obecná chemie*, chapter. 9. Elektrochemie, p. 249. Přírodovědecká fakulta, 2017.
12. De S., Dutta S., Saha B.: Catal. Sci. Tech. *6*, 7364 (2016).
13. Yu J., in book: *Studies in Surface Science and Catalysis* (Čejka J., van Bekkum H., Corma A., Schüth F., ed.), vol. *168*, p. 39. Elsevier, 2007.
14. Grand J., Awala H., Mintova S.: CrystEngComm *18*, 650 (2016).
15. Maldonado M., Oleksiak M. D., Chinta S., Rimer J. D.: J. Am. Chem. Soc. *135*, 2641 (2013).
16. Castañeda R., Corma A., Fornés V., Martínez-Triguero J., Valencia S.: J. Catal. *238*, 79 (2006).
17. Corma A., Rey F., Valencia S., Jordá J. L., Rius J.: Nat. Mater. *2*, 493 (2003).
18. Chlubná-Eliášová P., Tian Y., Pinar A. B., Kubů M., Čejka J., Morris R. E.: Angew. Chem., Int. Ed. *53*, 7048 (2014).
19. Wells A. F., in book: *Structural Inorganic Chemistry*, p. 929. OUP Oxford, 2012.
20. Niedermeier C. A., Ide K., Katase T., Hosono H., Kamiya T.: J. Phys. Chem. C *124*, 25721 (2020).
21. O'Keeffe M., Yaghi O. M.: Chem. Eur. J. *5*, 2796 (1999).
22. Dawson C. J., Sanchez-Smith R., Rez P., O'Keeffe M., Treacy M. M. J.: Chem. Mater. *26*, 1523 (2014).
23. Jiang J., Yu J., Corma A.: Angew. Chem., Int. Ed. *49*, 3120 (2010).
24. Lim I. H., Schrader W., Schüth F.: Microporous Mesoporous Mater. *166*, 20 (2013).
25. Li Q., Navrotsky A., Rey F., Corma A.: Microporous Mesoporous Mater. *74*, 87 (2004).
26. Petkov P. S., Aleksandrov H. A., Valtchev V., Vayssilov G. N.: Chem. Mater. *24*, 2509 (2012).
27. Eliášová P., Opanasenko M., Wheatley P. S., Shamzhy M., Mazur M., Nachtigall P., Roth W. J., Morris R. E., Čejka J.: Chem. Soc. Rev. *44*, 7177 (2015).
28. Rainer D. N., Rice C. M., Warrender S. J., Ashbrook S. E., Morris R. E.: Chem. Sci. *11*, 7060 (2020).
29. Zhou Y., Kadam S. A., Shamzhy M., Čejka J., Opanasenko M.: ACS Catal. *9*, 5136 (2019).

30.   Abdi S., Kubů M., Li A., Kalíková K., Shamzhy M.: Catal. Today *390-391*, 326 (2022).

31.   Zhang J., Veselý O., Tošner Z., Mazur M., Opanasenko M., Čejka J., Shamzhy M.: Chem. Mater. *33*, 1228 (2021).

32.   Shamzhy M. V., Opanasenko M. V., Ramos F. S. d. O., Brabec L., Horáček M., Navarro-Rojas M., Morris R. E., Pastore H. d. O., Čejka J.: Catal. Sci. Tech. *5*, 2973 (2015).

33.   Zhang J., Yue Q., Mazur M., Opanasenko M., Shamzhy M. V., Čejka J.: ACS Sust. Chem. Eng. *8*, 8235 (2020).

34.   Beckers M., Weise B., Kalapis S., Gries T., Seide G., Bunge C. A., in book: *Polymer Optical Fibres* (Bunge C.-A., Gries T., Beckers M., ed.), p. 9. Woodhead Publishing, 2017.

35.   Morris R. E., Wheatley P. S., in book: *Studies in Surface Science and Catalysis* (Čejka J., van Bekkum H., Corma A., Schüth F., ed.), vol. *168*, p. 375. Elsevier, 2007.

36.   Karge H. G., Hunger M., Beyer H. K., in book: *Catalysis and Zeolites: Fundamentals and Applications* (Weitkamp J., Puppe L., ed.), p. 198. Springer Berlin Heidelberg, Berlin, Heidelberg 1999.

37.   Susanne S., Timothy R., in book: *Advances in Microfluidics and Nanofluids* (Murshed S. M. S., ed.), Ch. 2. IntechOpen, Rijeka 2020.

38.   https://microbiologyinfo.com/differences-between-light-microscope-and-electron-microscope/, download (15. 1. 2023)

39.   Kogure T.: Dev. Clay Sci. *5*, 275 (2013).

40.   Cychosz K. A., Guillet-Nicolas R., García-Martínez J., Thommes M.: Chem. Soc. Rev. *46*, 389 (2017).

41.   Thommes M., Kaneko K., Neimark A. V., Olivier J. P., Rodriguez-Reinoso F., Rouquerol J., Sing K. S. W.: Pure and Applied Chemistry *87*, 1051 (2015).

42.   Rahman, M. M.; Muttakin, M.; Pal, A.; Shafiullah, A. Z.; Saha, B. B. A Statistical Approach to Determine Optimal Models for IUPAC-Classified Adsorption Isotherms Energies *12*, no. 23: 4565., 2019.

43.   Lippens B. C., de Boer J. H.: J. Catal. *4*, 319 (1965).

44.   McDonald R. S.: Anal. Chem. *54*, 1250 (1982).

45.   Lercher J. A., Jentys A., in book: *Studies in Surface Science and Catalysis* (Čejka J., van Bekkum H., Corma A., Schüth F., ed.), vol. *168*, p. 435. Elsevier, 2007.

46.   Bordiga S., Lamberti C., Bonino F., Travert A., Thibault-Starzyk F.: Chem. Soc. Rev. *44*, 7262 (2015).

47.   Cejka J., Vondrova A., Wichterlova B., Vorbeck G., Fricke R.: Zeolites *14*, 147 (1994).

48.   Coudurier G., Védrine J. C., in book: *Studies in Surface Science and Catalysis* (Murakami Y., Iijima A., Ward J. W., ed.), vol. 28., p. 643. Elsevier, 1986.

49.   Jentys A., Lercher J. A., in book: *Studies in Surface Science and Catalysis* (van Bekkum H., Flanigen E. M., Jacobs P. A., Jansen J. C., ed.), vol. 137, p. 345. Elsevier, 2001.

50.   Shamzhy M., Přech J., Zhang J., Ruaux V., El-Siblani H., Mintova S.: Catal. Today *345*, 80 (2020).

51.   Joshi H., Ochoa-Hernández C., Nürenberg E., Kang L., Wang F. R., Weidenthaler C., Schmidt W., Schüth F.: Microporous Mesoporous Mater. *309*, 110566 (2020).

52.   Wichterlová B., Tvarůžková Z., Sobalík Z., Sarv P.: Microporous Mesoporous Mater. *24*, 223 (1998).

53.   Mäntele W., Deniz E.: Spectrochim. Acta A *173*, 965 (2017).

54.   Nogier J.-P., Millot Y., Man P. P., Shishido T., Che M., Dzwigaj S.: J. Phys. Chem. C *113*, 4885 (2009).

55.   Ramanathan A., Castro Villalobos M. C., Kwakernaak C., Telalovic S., Hanefeld U.: Chem. Eur. J. *14*, 961 (2008).

56. Liu M., Jia S., Li C., Zhang A., Song C., Guo X.: Chinese Journal of Catalysis *35*, 723 (2014).
57. Corma A., Puche M., Rey F., Sankar G., Teat S. J.: Angew. Chem., Int. Ed. *42*, 1156 (2003).
58. Lakiss L., Vicente A. é., Gilson J. P., Valtchev V., Mintova S., Vimont A., Bedard R., Abdo S., Bricker J.: ChemPhysChem *21*, 1873 (2020).
59. Pitínová-Štekrová M., Eliášová P., Weissenberger T., Shamzhy M., Musilová Z., Čejka J.: Catal. Sci. Tech. *8*, 4690 (2018).
60. Harris J. W., Cordon M. J., Di Iorio J. R., Vega-Vila J. C., Ribeiro F. H., Gounder R.: J. Catal. *335*, 141 (2016).
61. Antić Ž., Krsmanović R. M., Nikolić M. G., Marinović-Cincović M., Mitrić M., Polizzi S., Dramićanin M. D.: Mater. Chem. Phys. *135*, 1064 (2012).
62. Debataraja A., Zulhendri D. W., Yuliarto B., Nugraha, Hiskia, Sunendar B.: Procedia Engineering *170*, 60 (2017).
63. Kasneryk V. I., Shamzhy M. V., Opanasenko M. V., Čejka J.: Journal of Energy Chemistry *25*, 318 (2016).
64. Shamzhy M. V., Eliašová P., Vitvarová D., Opanasenko M. V., Firth D. S., Morris R. E.: Chem. Eur. J. *22*, 17377 (2016).
65. Shamzhy M., Gil B., Opanasenko M., Roth W. J., Čejka J.: ACS Catal. *11*, 2366 (2021).
66. Podolean I., Zhang J., Shamzhy M., Pârvulescu V. I., Čejka J.: Catal. Sci. Tech. *10*, 8254 (2020).